Title

Rapid shelf-wide cooling response of a stratified coastal ocean to hurricanes

Authors

Greg Seroka[1], Travis Miles[1], Yi Xu[2], Josh Kohut[1], Oscar Schofield[1], Scott Glenn[1]

[1]Center for Ocean Observing Leadership, Department of Marine and Coastal Sciences, School of Environmental and Biological Sciences, Rutgers University, New Brunswick, NJ 08901 USA

[2]State Key Laboratory of Estuarine and Coastal Research, East China Normal University, 3663 Zhongshan Road North, Shanghai 200062, China

Corresponding Author: Greg Seroka, Ocean Prediction Center, NOAA/NWS/NCEP, 5830 University Research Court, College Park, MD 20740 (gregory.seroka@noaa.gov)

Key Points:

1: Observations, models reveal similar processes governing stratified coastal ocean cooling response to Hurricane Irene, Tropical Storm Barry

2: Robust shear-induced mixing produced rapid ahead-of-eye-center cooling in TCs on opposite ends of track & seasonal stratification envelope

3: Coupled TC models capable of predicting processes leading to rapid cooling of stratified coastal oceans critical for populated coastlines

Index Terms:

3372 Tropical cyclones, 4217 Coastal processes, 4255 Numerical modeling, 4572 Upper ocean and mixed layer processes, 4263 Ocean predictability and prediction

Keywords:

hurricanes, tropical cyclones, coastal oceanography, ocean modeling, gliders, continental shelf processes

Abstract

Large uncertainty in the predicted intensity of tropical cyclones (TCs) persists compared to the steadily improving skill in the predicted TC tracks. This intensity uncertainty has its most significant implications in the coastal zone, where TC impacts to populated shorelines are greatest. Recent studies have demonstrated that rapid ahead-of-eye-center cooling of a stratified coastal ocean can have a significant impact on hurricane intensity forecasts. Using observation-validated, high-resolution ocean modeling, the stratified coastal ocean cooling processes observed in two U.S. Mid-Atlantic hurricanes were investigated: Hurricane Irene (2011)—with an inshore Mid-Atlantic Bight (MAB) track during the late summer stratified coastal ocean season—and Tropical Storm Barry (2007)—with an offshore track during early summer. For both storms, the critical ahead-of-eye-center depth-averaged force balance across the entire MAB shelf included an onshore wind stress balanced by an offshore pressure gradient. This resulted in onshore surface currents opposing offshore bottom currents that enhanced surface to bottom current shear and turbulent mixing across the thermocline, resulting in the rapid cooling of the surface layer ahead-of-eye-center. Because the same baroclinic and mixing processes occurred for two storms on opposite ends of the track and seasonal stratification envelope, the response appears robust. It will be critical to forecast these processes and their implications for a wide range of future storms using realistic 3D coupled atmosphere-ocean models to lower the uncertainty in predictions of TC intensities and impacts and enable coastal populations to better respond to increasing rapid intensification threats in an era of rising sea levels.

1. Introduction

Although substantial progress in the prediction of tropical cyclone (TC) tracks has been realized globally over the past few decades, TC intensity prediction skill has remained comparatively flat across all TC ocean basins [*DeMaria et al.*, 2014; *Sopko and Falvey*, 2014; *Cangialosi and Franklin*, 2016]. This intensity gap can be traced to high resolution requirements for TC models, poor understanding and modeling of the atmospheric boundary layer, difficulty for many existing assimilation techniques to ingest observations of small but intense features, and—most importantly for this study—challenges in modeling the upper ocean response to TCs [*Emanuel*, 2016 and references within]. Large uncertainty in predicting the strength of TCs thus remains, which has its most significant implications for landfalling TCs where impacts to life and property—via storm surge, wind damage, and inland flooding—are greatest. These storms must first traverse the shallow, coastal ocean before making landfall. The number of studies in the literature investigating shallow, coastal ocean TC responses, indeed, pales in comparison to the number examining deep, open ocean TC responses [*Seroka et al.*, 2016]. Further, the differences between the deep, open ocean processes and the coastal processes are stark due to the influence of the bottom boundary layer and coastal wall in shallow water [*Glenn et al.*, 2016; *Seroka et al.*, 2016]. It is critical to close this gap, with the goal of improving the simulation of coastal ocean physics in coupled TC intensity models [e.g. *Zambon et al.*, 2014; *Warner et al.*, 2017].

In the summer hurricane season, the shallow Mid Atlantic Bight (MAB) off the U.S. East Coast is one of the most seasonally-stratified regions in the world [*Schofield et al.*, 2008], characterized by a sun-heated warm (>25°C) and thin (10m or less) surface

76 layer and a cold (<10°C) bottom layer termed the "Cold Pool" [*Houghton et al.*, 1982].
77 When Hurricane Irene traversed the highly stratified, shallow MAB waters in August
78 2011 before making landfall in New Jersey, rapid surface cooling caused by mixing
79 processes resulting from the two-layer baroclinic circulation in the MAB were observed
80 by an underwater glider and several National Data Buoy Center (NDBC) buoys; these
81 intense mixing processes and the surface cooling (up to 11°C) response in the MAB are
82 described in detail in Glenn et al. [2016]. Because the magnitude of the cooling was so
83 significant, it led to a reversal in the direction of air-sea latent and sensible heat fluxes—
84 from the ocean providing heat to the storm when using a fixed pre-storm warm sea
85 surface temperature (SST) bottom boundary condition to the ocean acting as a heat sink
86 when using the fixed post-storm cold SST condition [*Seroka et al.*, 2016].
87 This cooling was also found to primarily occur ahead of Irene's eye center—
88 critical for direct impact on storm intensity—as the storm traversed northeastward along
89 the MAB coastline. The cascade of processes responsible were strong ahead-of-eye-
90 center onshore winds and surface currents, coastal setup with water piling up along the
91 coast, offshore bottom currents in response to the resulting offshore pressure gradient,
92 and larger shear-driven turbulence, mixing, and entrainment of cold bottom water to the
93 surface due to directly opposing onshore surface and offshore bottom currents.
94 The ahead-of-eye-center cooling signal that resulted from these baroclinic coastal
95 ocean mixing processes was found to be present in the ten additional storms since 1985
96 that traversed northeastward across the MAB in the summer stratified season, and also in
97 Super Typhoon Muifa (2011) in the similarly highly-stratified Yellow Sea between
98 eastern China and Korea. Further, this ahead-of-eye-center cooling was found to have a

large impact on Hurricane Irene's intensity, larger than any other Weather Research and Forecasting (WRF) parameter tested [*Seroka et al.*, 2016].

Many questions remain. First, it is not known to what extent the ahead-of-eye-center cooling impacted the intensities of the other ten MAB storms and Typhoon Muifa. Extensive sensitivity studies like the one performed by Seroka et al. [2016] would need to be conducted for each storm to investigate these intensity impacts.

Second, it is not known if the same or different cooling processes occurred in the other ten MAB storms and in Typhoon Muifa. To improve understanding of TC coastal ocean response, the dominant momentum balances that occurred in these storms as well as mixing vs. advective processes that led to the ahead-of-eye-center cooling signals should be investigated in detail. It is also critical to understand the spatial—cross- and along-shelf, shallow and deep water—variability of the cooling processes, for a wider range of storms including Irene. Previous studies focused on these processes at the underwater glider location and not elsewhere on the MAB continental shelf [i.e. *Glenn et al.*, 2016]. These research gaps will guide this paper's work.

Standard operational model annual performance metrics are based on the mean across all storms simulated during one or several hurricane seasons (e.g. [*Kim et al.*, 2014; *Tallapragada et al.*, 2014; *Cangialosi and Franklin*, 2016]). While this method is effective in testing overall performance of a model, it tends to wash out any unique storm characteristics in both the atmosphere and the ocean. The full range of storm characteristics represents the full range of storm air-sea feedbacks that coupled models should capture and resolve. Therefore, it is critical to not only improve models incrementally based on the mean in an operational environment (e.g. [*Kim et al.*, 2014;

122 *Tallapragada et al.*, 2014; *Cangialosi and Franklin*, 2016]), but also to investigate
123 individual case studies and processes that models may or may not be correctly resolving
124 (e.g. [*D'Asaro et al.*, 2007; *Lin et al.*, 2009; *Jaimes and Shay*, 2015; *Glenn et al.*, 2016;
125 *Seroka et al.*, 2016]).

126 In order to better understand the baroclinic ocean response for different storms,
127 further investigation was performed on Irene and Tropical Storm Barry (2007), one of the
128 other ten MAB storms listed in Glenn et al. [2016]. A map of National Hurricane Center
129 (NHC) best tracks for Irene and Barry show both storms traversing northeastward over
130 the MAB, with Irene traveling 600km from eastern North Carolina (NC) to New York
131 City in 19 hours in late August 2011 (~32 km/h translation speed), and Barry traveling
132 700km from eastern NC to just south of Montauk Point, NY in 18 hours in early June
133 2007 (~39 km/h translation speed, Fig. 1, left). Typical translation speeds at MAB
134 latitudes are 29-36 km/h [*Mei et al.*, 2012]. Intensity time series show Irene weakening
135 throughout its MAB crossing using both wind and pressure intensity metrics, and show
136 Barry weakening—at a lesser rate than Irene—over its last 12 hours across the MAB
137 using both metrics (Fig. 1, right). Both storms had a radius of maximum wind (RMW)
138 reported in the Automated Tropical Cyclone Forecast [ATCF; *Sampson and Schrader*,
139 2000] system database of ~74 km 30 hours prior to storm presence over eastern NC, with
140 Irene's RMW increasing to 185 km 36 hours later when the storm was over the MAB.
141 For context, the average RMW for hurricanes making landfall in the U.S. from 1893 to
142 1979 was 47 km [*Hsu and Yan*, 1998].

143 For both of these storms, Rutgers University underwater gliders were deployed on
144 the MAB continental shelf. Irene had a more inshore track northward through the MAB

and Barry tracked farther offshore along the shelf break (Fig. 1). Irene occurred in late August toward the end of the MAB summer stratified season, while Barry occurred in early June, during the beginning of the summer stratified season. However, the intent is not to perform direct comparisons between the two storms, as this would introduce several uncontrollable variables and not be a fully controlled experiment. Rather, the objective is to better understand the conditions in both the atmosphere and ocean that may lead to the baroclinic coastal ocean cooling processes, ahead-of-eye-center cooling, and impact on storm intensities for two extremes in the storm track—one nearshore and one well offshore—and two extremes in summer stratification—one near the end and one near the beginning of the season. This paper will investigate the details of and variability in the dominant baroclinic coastal ocean processes—in both the cross- and along-shelf directions—for both Irene and Barry. By studying the spatiotemporal variability in these baroclinic coastal ocean cooling TC processes, the aim will be to improve the modeling of the full range of stratified coastal ocean TC responses.

2. Data and Methods

2.1 High Frequency (HF) Radar

Hourly surface ocean current data, one-hour center-averaged, from a network of CODAR Ocean Sensors SeaSonde HF Radar stations [*Roarty et al.*, 2010] along the MAB coast were used in this paper. Surface current map data have a nominal 6km spatial resolution (Fig 1).

2.2 Gliders

Teledyne-Webb Research (TWR) Slocum gliders, autonomous underwater vehicles (AUVs), were used in this paper [*Schofield et al.*, 2007; *Glenn et al.*, 2008,

168 2016; *Ruiz et al.*, 2012; *Miles et al.*, 2013, 2015]. Rutgers University Gliders RU16
169 (Irene) and RU17 (Barry) data were analyzed. Both gliders were equipped with a Seabird
170 unpumped conductivity, temperature, and depth (CTD) sensor.
171 Depth- and time-averaged velocity calculations were performed using a dead-
172 reckoning technique, a method typically used for underwater gliders [*Sherman et al.*,
173 2001; *Davis et al.*, 2002; *Schofield et al.*, 2007]. To estimate bottom layer currents at the
174 glider location, a combination of dead-reckoned depth-averaged glider currents and HF
175 radar surface currents is used (Fig. 2). This method assumes that the HF radar surface
176 currents are representative of the currents in the surface mixed layer above the
177 thermocline. See [*Glenn et al.*, 2016] for detailed methods and equations used to calculate
178 bottom layer currents.
179 **2.3 Bathymetry**
180 U.S. Coastal Relief Model data from the NOAA National Centers for
181 Environmental Information were used for water depth and coastlines throughout this
182 paper [*NOAA National Centers for Environmental Prediction*, 2016].
183 **2.4 Satellite SST**
184 Advanced Very High Resolution Radiometer (AVHRR) data were used for ocean
185 model SST verification. Techniques empirically-derived for the MAB to remove bright
186 cloud covered pixels and retain darker ocean pixels were used to decloud AVHRR data
187 but preserve the rapid TC cooling signal, following [*Glenn et al.*, 2016].
188 **2.5 Regional Ocean Modeling System (ROMS): ESPreSSO**
189 Ocean model simulations were conducted using ROMS [*Haidvogel et al.*, 2008], a
190 free-surface, sigma coordinate, primitive equation ocean model (code available at

191 http://www.myroms.org). ROMS has been used for a wide variety of coastal applications.
192 Specifically, the ESPreSSO (Experimental System for Predicting Shelf and Slope Optics)
193 model [*Wilkin and Hunter*, 2013], covering the MAB from Cape Cod to south of Cape
194 Hatteras, and from the inland bays to beyond the shelf break, was used for simulations. In
195 an assessment of skill of real-time ocean models over the MAB continental shelf for
196 2010-2011, ESPreSSO performed well as compared to global models and other regional
197 models, indicating its usefulness for simulating coastal ocean circulations across a wide
198 range of conditions, including Hurricane Irene which also occurred in 2011 [*Wilkin and*
199 *Hunter*, 2013].
200 The ESPreSSO grid has a horizontal resolution of 5km and 36 vertical levels in a
201 terrain-following s-coordinate system. Initial conditions here were developed from an
202 ESPreSSO grid ROMS reanalysis with strong constrained four-dimensional variational
203 (4D-Var) data assimilation, including assimilation of sea surface height, SST, HF radar
204 surface currents, and in situ temperature and salinity observations, For atmospheric
205 forcing, North American Mesoscale (NAM) 12km 3-hourly forecast data from its daily
206 00Z cycles were used. Only short-term forecast hours f03-f27 were used to limit any
207 longer term forecast error, with the f00 analysis skipped to allow for model spinup. NAM
208 surface air temperature, pressure, relative humidity, 10m vector winds, precipitation,
209 downward longwave radiation, and net shortwave radiation were used to specify the
210 surface momentum and buoyancy fluxes based on the COARE bulk formulae [*Fairall et*
211 *al.*, 2003].
212 The NAM track map and intensity time series as assembled here for both Irene
213 and Barry are compared to the NHC best track analyses (Fig. 1). NHC best track

214 uncertainty estimates depend on the intensity of the TC, with the uncertainty increasing
215 as the intensity decreases [*Torn and Snyder*, 2012]. For both storms, the NAM tracks are
216 all well within or just outside the best track uncertainties, and the NAM maximum wind
217 intensities are within or at the best track uncertainties (Fig. 1). For Barry, the minimum
218 central pressure intensities are well within the uncertainties, and for Irene, they are at or
219 just outside the uncertainties. The wind rather than central pressure intensities are most
220 relevant for this study, as the winds provide the momentum fluxes forcing the TC ocean
221 response. Overall, the NAM tracks properly represent the typical MAB track envelope,
222 with Irene propagating along the inner shelf and Barry along the mid to outer shelf.
223 Boundary conditions were daily two-dimensional surface elevation and three-
224 dimensional velocity, temperature, and salinity fields from the Hybrid Coordinate Ocean
225 Model (HYCOM) Navy Coupled Ocean Data Assimilation (NCODA) forecast system.
226 River inflows were from the seven largest rivers, using daily average U.S.G.S. discharge
227 data. Tidal boundary conditions were from the ADvanced CIRCulation (ADCIRC) tidal
228 model. Finally, vertical turbulence diffusivity was determined using the general length
229 scale method k-kl type vertical mixing scheme [*Umlauf and Burchard*, 2003; *Warner et*
230 *al.*, 2005].
231 For Barry, the ROMS ESPreSSO simulation was initialized at 1200 UTC on May
232 29, 2007 and ended at 1200 UTC on June 8, 2007, with storm eye passage by glider
233 RU17 at 1700 UTC on June 4, 2007, just over five days into the simulation to allow for
234 model spin-up. For Irene, the ROMS ESPreSSO simulation was initialized at 1200 UTC
235 on August 24, 2011 and ended at 0000 UTC on September 3, 2011, with storm eye

passage by glider RU16 at 1200 UTC on August 28, 2011, exactly four days into the simulation.

The depth-averaged momentum balance terms were direct output from the ROMS simulations, and the equations are as follows:

$$\underbrace{\frac{\partial u}{\partial t}}_{\text{acceleration}} = \underbrace{-\frac{\partial(uu)}{\partial x} - \frac{\partial(vu)}{\partial y}}_{\text{horizontal advection}} \underbrace{-\frac{1}{\rho_0}\frac{\partial P}{\partial x}}_{\text{pressure gradient}} + \left(\underbrace{\frac{\tau_s^x}{h\rho_0}}_{\text{surface stress}} - \underbrace{\frac{\tau_b^x}{h\rho_0}}_{\text{bottom stress}}\right) + \underbrace{fv}_{\text{Coriolis}} \tag{1}$$

$$\underbrace{\frac{\partial v}{\partial t}}_{\text{acceleration}} = \underbrace{-\frac{\partial(uv)}{\partial x} - \frac{\partial(vv)}{\partial y}}_{\text{horizontal advection}} \underbrace{-\frac{1}{\rho_0}\frac{\partial P}{\partial y}}_{\text{pressure gradient}} + \left(\underbrace{\frac{\tau_s^y}{h\rho_0}}_{\text{surface stress}} - \underbrace{\frac{\tau_b^y}{h\rho_0}}_{\text{bottom stress}}\right) - \underbrace{fu}_{\text{Coriolis}} \tag{2}$$

where u and v are the along-shelf and cross-shelf components of depth-averaged velocity respectively, t is time, P is depth-averaged pressure, ρ_o is a reference density, τ_s and τ_b are surface (wind) and bottom stresses, h is water column depth, and f is the latitude-dependent Coriolis frequency. Horizontal diffusion was small and neglected here.

The temperature rate equation terms to diagnose advection vs. mixing were also direct output from ROMS. The equation is as follows:

$$\frac{\partial T}{\partial t} = -\frac{\partial(uT)}{\partial x} - \frac{\partial(vT)}{\partial y} - \frac{\partial(wT)}{\partial z} + \frac{\partial A_{kt}\frac{\partial T}{\partial z}}{\partial z} + D_T + F_T \tag{3}$$

with the following surface and bottom boundary conditions, respectively:

$$\left(A_{kt}\frac{\partial T}{\partial z}\right)_{z=0} = \frac{Q_{net}}{\rho_0 C_p} \tag{4}$$

$$\left(A_{kt}\frac{\partial T}{\partial z}\right)_{z=0} = 0 \tag{5}$$

255 Here, T is the temperature, t is time, u, v, and w are the along-shelf, cross-shelf and
256 vertical components of velocity. A_{kt} is the vertical diffusivity coefficient, D_T is the
257 horizontal diffusion term and F_T is friction. Q_{net} is the surface net heat flux, ρ_0=1025,
258 kg m^{-3} is a reference density, C_p=3985 J (kg °C)$^{-1}$ is the specific heat capacity of
259 seawater and h is the water depth. Horizontal diffusion again was small and neglected
260 here.

261 **3. Results**

262 **3.1 Observations**

263 Glenn et al. [2016] used HF radar and glider RU16 data to determine surface,
264 depth-averaged, and bottom currents at the glider location during Irene. Part of the time
265 series is repeated here in Fig. 2 for ease of comparison to a similar analysis for Barry. At
266 0600 UTC on August 28, 2011, less than four hours before Irene's NJ landfall and eye
267 passage by glider RU16, surface ocean currents were directed onshore and upshelf,
268 aligning close to the onshore winds ahead of Irene's eye (Fig. 2, top left). Current
269 magnitudes at this time approached 1 m s^{-1}. At 0200 UTC on June 4, 2007, a full 15
270 hours before Barry's eye passage by glider RU17, surface ocean currents were in a very
271 similar direction, onshore and upshelf.

272 Time series of temperature profiles at the glider locations below the surface
273 current maps indicate initially very strong stratification and an eventual breakdown in
274 stratification upon storm forcing. For Irene in late August, surface mixed layer
275 temperatures approached 25°C to ~10-15m depth, and bottom MAB Cold Pool
276 temperatures were less than 10°C. For Barry in early June, surface mixed layer
277 temperatures down to ~10-15m depth were approaching 16°C with bottom MAB Cold

278 Pool temperatures again less than 10°C, approaching 5°C. For Irene, the thermocline
279 (black contour) deepened to ~30m depth and surface mixed layer temperatures cooled to
280 ~17°C, with much (~5°C, or ~75%) of the cooling occurring ahead-of-eye-center. For
281 Barry, the thermocline (black contour) deepened briefly to 25m depth and surface mixed
282 layer temperatures cooled to nearly 14°C, with 100% of the cooling at RU17 occurring
283 ahead-of-eye-center.

284 Cross-shelf and along-shelf surface (red), depth-averaged (green), and bottom
285 (blue) current time series are depicted in the two panels below the temperature time series
286 in Fig. 2. For Irene, currents in Earth coordinates are rotated 31° clockwise from north to
287 attain cross- and along-shelf components. For Barry, currents in Earth coordinates are
288 rotated 50° clockwise from north to attain cross- and along-shelf components. For both
289 Irene and Barry, red surface currents peaked onshore ahead-of-eye-center, and blue
290 bottom currents peaked offshore at the same time yet with a bit of a lag in set up. For
291 Irene, along-shelf currents were very small ahead-of-eye-center, but for Barry, along-
292 shelf surface currents to the northeast peaked ahead-of-eye-center and bottom currents
293 peaked just before. For both storms, observations indicate a two-layer circulation, with
294 cross-shelf surface currents onshore and cross-shelf bottom currents offshore, enhancing
295 the shear and resultant mixing and cooling. For Barry, a similar surface to bottom shear
296 profile occurred in the along-shelf direction. The bottom right panel in Fig. 2 shows a
297 calculation of surface to bottom shear, combining both the along- and cross-shelf
298 components for Barry due to the large observed along-shelf component. Maximum shear
299 occurred at the same time as maximum surface cooling and thermocline deepening, and
300 well before eye passage.

301 **3.2 Modeling**

302 In order to investigate the details of the baroclinic processes and mixing that
303 occurred in Irene and Barry, including momentum balance analysis and the temperature
304 diagnostic equation for mixing vs. advection comparisons, ROMS ESPreSSO simulations
305 were performed as described in Section 2.5 above.

306 **3.2.1 ROMS Simulation Validation: Hurricane Irene (2011)**

307 A pre-storm map of SST over the MAB from AVHRR at 0742 UTC on August
308 24, 2011 (Fig. 3, top left) shows coastal upwelling along the NJ, DE, and MD coastlines,
309 with a warm tongue of SST through the southern MAB and extending offshore of the
310 50m isobath and into the northern MAB north of the Hudson Canyon. The ROMS
311 ESPreSSO re-run SST ~four hours later (Fig. 3, top right) shows very good agreement
312 with AVHRR, capturing the coastal upwelling, warm tongue, Gulf Stream, and colder
313 waters south of Rhode Island and Nantucket.

314 A post-storm map of SST over the MAB from AVHRR at 0828 UTC on August
315 29, 2011 (Fig. 3, middle left) shows a much different story, with cold <18°C SST from
316 the mouth of the Hudson Canyon and northward, and a corridor of colder water at the
317 50m isobath and offshore in the southern MAB. The ROMS ESPreSSO re-run SST (Fig.
318 3, middle right) again shows very good agreement with AVHRR, with perhaps the only
319 minor issue being not as cold water at the mouth of the Delaware Bay and in the southern
320 MAB.

321 A difference map of post-storm minus pre-storm AVHRR SST (Fig. 3, bottom
322 left) shows maximum cooling (approaching 11°C) at the mouth of the Hudson Canyon
323 and across the MAB, with less cooling in the shallow regions of the shelf and offshore in

the deep water. Again, ROMS (Fig. 3, bottom right) agrees very well with the AVHRR cooling map, capturing the maximum in cooling at the Hudson Canyon mouth.

Finally, RU16 glider temperature profile time series (Fig. 4, left) shows the same deepening of the thermocline and cooling of the surface layer as shown in Fig. 2. ROMS (Fig. 4, right) taken at the closest grid cell to the average position of RU16 during the storm period shows an initial thermocline ~10-15m too deep but with correct surface mixed layer and bottom layer temperatures. Although the simulated thermocline is deeper than observed, the two-layer structure is present to support the relevant processes. Upon storm forcing, the ROMS thermocline deepens to the correct depth, but the surface does not sufficiently cool, likely due to the inadequate supply of cold bottom water at the start. Insufficient surface ocean cooling in model simulations due to an excessively thick surface layer has also been found to occur in other recent TC studies [e.g. *Zhang et al.*, 2016], and is likely a common deficiency in numerical model simulations of TC ocean response. Despite deficiencies in the details, the overall storm response characteristics—two-layer structure at the start, deepening of the thermocline, and rapid and intense cooling of the surface mixed layer—are present and adequate for determining dominant force balances and diagnosing the causes of SST cooling.

3.2.2 ROMS Simulation Validation: Tropical Storm Barry (2007)

A pre-storm map of SST over the MAB from AVHRR at 0559 UTC on June 2, 2007 (Fig. 5, top left) is partially blocked by clouds but shows a warm Gulf Stream offshore, a couple Gulf Stream rings to the northwest in the slope water, a ribbon of colder water along the shelf break at 200m, a ribbon of warmer water inshore of the 50m isobath, and coastal upwelling east of Cape May, NJ, at the mouth of Delaware Bay, and

347 along the Delmarva Peninsula. ROMS (Fig. 5, top right) shows good agreement with
348 AVHRR, with a warm Gulf Stream, cold water to the north, NJ and Delaware Bay coastal
349 upwelling, warmer mid-shelf MAB waters, and a hint of the warm Gulf Stream filament
350 approaching the 200m isobath.

351 A post-storm map of SST over the MAB from AVHRR at 0207 UTC on June 5,
352 2007 (Fig. 5, middle left) with the same color bar as the top panels in Fig. 5 shows cooler
353 water over the northern MAB, and ROMS at the same time (Fig. 5, middle right)
354 provides a similar picture. The difference maps of post-storm minus pre-storm AVHRR
355 SST (Fig. 5, bottom left), ROMS re-run at the same time difference (Fig. 5, bottom
356 middle), and ROMS re-run to maximize cooling (Fig. 5, bottom right) highlight the
357 cooling and warming patterns across the MAB. Although clouds block parts of the map,
358 AVHRR shows a pattern of warming in the southern MAB and offshore, and cooling in
359 the northern MAB and offshore. Both ROMS re-run difference maps show more
360 widespread cooling, with slight warming offshore NJ and off the Delmarva Peninsula,
361 and where the Gulf Stream meanders moved through time.

362 Finally, the profile time series of temperature at the RU17 glider location (Fig. 6,
363 left) again shows surface mixed layer cooling and deepening during the storm period, as
364 in Fig. 2. ROMS ESPreSSO re-run (Fig. 6, right) shows a thermocline initially 15-20m
365 too deep, but surface and bottom temperatures overall correct. The resulting cooling of
366 the surface layer occurs at about the correct time, but the surface layer warming post-
367 storm does not occur.

368 **3.2.3 Temperature, current, shear, and momentum balance spatial time series: Irene**

369 At the cross section location near RU16 noted by the northwest to southeast black
370 dots in Fig. 3, Hövmoller diagrams of time (increasing up) vs. distance offshore were
371 produced. Surface temperature (Fig. 7, top left) shows initially warm surface water
372 stretching from the edge of the coastal upwelling to >200km offshore. Then, SST rapidly
373 cools across the shelf and in deep water, so that any cooling after eye passage (from
374 NAM—two hours later than observed) is minimal. No SST cooling occurred within the
375 nearshore coastal upwelling region. Bottom temperature (Fig. 7, bottom left) shows a
376 warm downwelling bulge during the storm, starting at the coastline and extending to
377 close to 50km offshore. The core of the MAB Cold Pool can be seen around 100km
378 offshore. Four sample locations are noted with the vertical solid lines labeled 1) in the
379 upwelling region, 2) near RU16, 3) in the core of the Cold Pool, and 4) in deep water.
380 These four locations will be used in the temperature diagnostic analysis, Section 3.2.5.
381 A Hövmoller of cross-shelf surface currents (Fig. 7, top middle) show onshore
382 currents increasing at about 0000 UTC on August 28, from about 50km offshore across
383 the shelf and into some of the deeper water. For Irene model results, currents in Earth
384 coordinates are again rotated 31° clockwise from north to attain cross- and along-shelf
385 components. The onshore surface currents peak at around 0300 UTC, and then decrease a
386 few hours before eye passage. Bottom currents (Fig. 7, bottom middle) are opposing
387 offshore across the shelf and weaker than the onshore surface currents. The bottom
388 onshore currents begin again at about 0000 UTC on August 28, and last until eye
389 passage. After eye passage, surface currents switch to offshore, with the switch nearshore
390 occurring a few hours after eye passage likely due to tidal influence (not shown). Bottom
391 currents switch to onshore after eye passage almost immediately. Maximum shear from

392 this plot occurred roughly from 0000 to 1200 UTC on August 28, and reversed from 1500
393 UTC on August 28 to 0000 UTC on August 29.

394 The along-shelf surface current Hövmoller (Fig. 7, top right) shows northeastward
395 currents ahead of and after eye passage, with southwestward surface currents after eye
396 passage in deeper water. Bottom currents (Fig. 7, bottom right) are southwestward ahead
397 of eye passage and immediately after, then northeastward later at 0000 UTC on August
398 29. Maximum shear from this plot occurred roughly from 0600 to 1500 UTC on August
399 28.

400 A bulk surface to bottom shear Hövmoller diagram, comprised of the cross- and
401 along-shelf components, is shown in Fig. 8 (left panel). This bulk shear Hövmoller shows
402 a symmetric ~50% ahead and 50% behind eye shear pattern in deep water, consistent
403 with Price [1981]. In the shallow water over the continental shelf, shear is skewed ahead-
404 of-eye-center. Because in deep water the bottom layer is quiescent and in shallow water
405 the bottom layer is moving, only qualitative comparisons between deep and shallow
406 water can be made. Additionally, bottom currents in shallow water are affected by
407 opposing bottom stress, restricting any quantitative comparisons between deep and
408 shallow water. By changing bottom currents to 0, a more evenly distributed shear pattern
409 between ahead of and behind eye passage results (Fig. 8, right), showing that the
410 opposing bottom currents in the two-layer circulation has an influence on the shear
411 pattern.

412 The ahead-of-eye-center cooling due to this shear is greater than behind-eye
413 cooling (Fig. 7, top left), potentially because 1) behind the eye center the water column is
414 already mixed, and the surface layer is already deeper, 2) there are weaker backside

offshore winds than front-side onshore winds due to frictional land effects—supported by observations at NDBC buoys 44014, 44009, and 44065, and at a WeatherFlow Inc. coastal land station at Tuckerton, NJ, and 3) the front side of Irene cools the SST, the eye moves over the cooler water and weakens the storm, and the backside is weaker (Fig. 1). As will be shown in the following momentum balance Hövmollers, the dominant cross-shelf momentum terms are onshore wind stress balanced by offshore pressure gradient force ahead-of-eye-center, and offshore wind stress balanced by onshore pressure gradient force behind-eye-center. This balance is likely due to the presence of the coastline and shallow bottom, in which onshore surface winds ahead-of-eye-center pile water at the coast and result in the offshore bottom current, and offshore surface winds behind-eye-center push water away from the coast and result in the onshore bottom current. In both cases—ahead-of-eye-center and behind-eye-center—a two-layer circulation occurs due to the presence of the coastline, shallow bottom, and stratified water column.

The depth-averaged cross-shelf momentum balance time series (Fig. 9) depicts all terms except for horizontal viscosity, which was very small. Acceleration shows a strongly tidal signal, with less onshore acceleration just before eye passage. Wind stress is strongly onshore ahead-of-eye passage, and switches to offshore after. Pressure gradient force is offshore ahead-of-eye-center from the coast all the way to the shelf break, and then switches to onshore mid-shelf first and then both nearshore and near the shelf break second; this pressure gradient pattern is due to coastal set up ahead-of-eye and coastal set down behind-eye. Coriolis is offshore, increasing after the eye. Bottom stress is onshore opposing the offshore bottom currents ahead-of-eye, and then switches sign

438 after eye. Finally, advection is small and noisy, with a response near the inertial period
439 especially near the shelf break. The dominant cross-shelf force balance progresses from
440 onshore wind stress balanced by offshore pressure gradient ahead-of-eye-center, to
441 offshore wind stress and Coriolis balanced by onshore pressure gradient after eye passage
442 until 0000 UTC on August 29, and finally to a geostrophic balance of offshore Coriolis
443 balanced by onshore pressure gradient.

444 In the along-shelf direction, depth-averaged momentum balance terms (Fig. 10)
445 are generally smaller than the cross-shelf terms. Again, acceleration has a tidal signal, but
446 so does Coriolis. The dominant along-shelf force balance progresses from southwestward
447 wind stress balanced by northeastward pressure gradient and Coriolis, to northeastward
448 wind stress balanced by southwestward pressure gradient and Coriolis, and finally to
449 alternating southwestward and northeastward pressure gradient balanced by Coriolis
450 (tidal periodicity).

451 **3.2.4 Temperature, current, shear, and momentum balance spatial time series:**
452 **Barry**

453 The time series of SST for Barry (Fig. 11, top left) was taken at the northern
454 WNW to ESE cross section location just north of the Hudson Canyon as indicated by the
455 black dots in Fig. 5. This northern location was chosen to target the greatest SST cooling
456 in Barry. A similar cooling signal is apparent across the shelf and even in deep water. At
457 National Data Buoy Center (NDBC) station ALSN6, the Barry station used by [*Glenn et*
458 *al.*, 2016] for the ahead-of-eye-center cooling signal, cooling (~3.5°C) was greatest. At
459 the warm strip of water indicated by the vertical line labeled "2", and in the deep water,
460 total cooling was less than 1°C. The bottom temperature spatial time series (Fig. 11,

461 bottom left) shows a similar but more subtle downwelling bulge from the coast as was
462 evident in Irene. Five sample locations are noted with the vertical solid lines labeled 1) in
463 the nearshore maximum cooling and near ALSN6, 2) in the warm strip of water, 3) in the
464 core of the Cold Pool, 4) near RU17, and 5) in deep water. These five locations will be
465 used in the temperature diagnostic analysis, Section 3.2.6.

466 The cross-shelf surface current time series (Fig. 11, top middle) shows onshore
467 surface currents peaking 12-18 hours prior to eye passage, but remaining weakly onshore
468 until eye passage. For Barry model results, currents in Earth coordinates are again rotated
469 51° clockwise from north to attain cross- and along-shelf components. Bottom currents
470 (Fig. 11, bottom middle) show a primarily tidal signal, with alternative offshore and
471 onshore bottom currents. Maximum shear was roughly 0600 to 1200 UTC on June 4.
472 This maximum shear occurs when the bottom offshore currents (mainly tidal) oppose the
473 onshore surface currents. Because the storm forcing is weaker than in Irene, the tidal
474 signal dominates the bottom current forcing. This is consistent with the findings of Keen
475 and Glenn [1995], who found that during a storm crossing the MAB in October 1990, the
476 tidal signal dominated the bottom current forcing, and storm sedimentation was directly
477 related to the tidal flow.

478 In the along-shelf direction, surface currents were northeastward before eye
479 passage and southwestward after (Fig. 11, top right). Bottom currents were
480 southwestward the entire storm period, both before and after eye passage. A similar
481 analysis just south of the Hudson Canyon may help answer why this occurred. One
482 potential reason is that the Hudson Canyon acted as a barrier, blocking bottom currents
483 from crossing the large bathymetric gradients.

484 The bulk surface to bottom shear Hövmoller for Barry, comprised of the cross-
485 and along-shelf shears, is shown in Fig. 12 (left panel). This bulk shear Hövmoller again
486 shows a roughly symmetric ~50% ahead and 50% behind eye shear pattern in deep water
487 if the time period of 0000 UTC on June 4 to 0600 UTC on June 5 is used. Again, like for
488 Irene, shear is skewed ahead-of-eye passage in the shallow water, and by substituting 0
489 for bottom currents, a more (but not quite fully) symmetric shear pattern in shallow water
490 results (Fig. 12, right).
491 The Hövmoller cross-shelf depth-averaged momentum balance terms (Fig. 13)
492 show a strongly tidal signal in the acceleration, pressure gradient, and Coriolis terms
493 across the shelf, and in the bottom stress and horizontal advection terms very near shore.
494 Wind stress was directed onshore ahead of eye passage and weakly offshore after.
495 Pressure gradient was primarily tidal, with more positive offshore values along the shelf
496 break just ahead of eye passage as compared to after eye passage. Coriolis was largely
497 tidal and onshore, with the maximum again at the shelf break. Bottom stress was mostly
498 tidal, but mostly negative opposing the offshore bottom currents at about 0600 UTC on
499 June 4 ahead of eye, when the downwelling circulation aligned with the tidal signal.
500 Finally, horizontal advection was mostly small. The dominant depth-averaged cross-shelf
501 force balance progressed from onshore wind stress balanced by offshore pressure
502 gradient ahead of eye passage, to offshore wind stress balanced by alternating
503 onshore/offshore Coriolis and pressure gradient (tidal periodicity) just after eye passage,
504 to quasi-geostrophic balance with alternating onshore/offshore Coriolis balanced by
505 pressure gradient (again tidal).

506 The Hövmoller along-shelf depth-averaged momentum balance terms (Fig. 14)
507 show a mostly tidally-forced signature. Acceleration was mostly tidal, with slightly more
508 negative onshore (or less positive offshore) acceleration ahead of eye passage from 0000
509 to ~0900 UTC on June 4. Wind stress was southwestward ahead of eye passage and
510 northeastward after. Pressure gradient and Coriolis terms were primarily tidal, bottom
511 stress was always northeastward opposing the southwestward bottom currents, and
512 horizontal advection was small. The dominant along-shelf depth-averaged momentum
513 balance progressed from southwestward wind stress balanced by northeastward bottom
514 stress and a residual in the alternating northeastward/southwestward pressure gradient
515 term and Coriolis term ahead of eye passage, to northeastward wind stress balanced by
516 alternating northeastward/southwestward Coriolis and pressure gradient behind eye
517 passage.
518 The shelf break maxima in the pressure gradient and Coriolis terms could be due
519 to the presence of a warm core ring starting pre-storm just north of the Hudson Canyon
520 and the northern cross section location (Fig. 5, top left) and moving southeastward by
521 post-storm (Fig. 5, middle left). This ring, moving along the shelf break and beginning to
522 impinge onto the shelf, forces a geostrophic circulation at the shelf break front [*Zhang*
523 *and Gawarkiewicz*, 2015], which is evident at the shelf break in both the cross- and
524 along-shelf momentum balance Hövmollers (Figs. 12 and 13).
525 **3.2.5 Advection vs. Mixing Temperature Response: Irene**
526 The temperature diagnostic equation terms were plotted for Irene (Fig. 15) at the
527 points indicated by the large red dots on Fig. 3 and by the vertical solid black lines on the
528 left panels of Fig. 7 to determine the primary cause of cooling. The left panel is within

529 the upwelling region, the second is at RU16, the third is in the MAB Cold Pool core, and
530 the fourth is in deep water. At the top is the full temperature rate term, in the middle is
531 the vertical diffusion term, and at the bottom are the vertical plus horizontal advection
532 terms. Horizontal diffusion was not plotted, as it was very small. First, a general tidal
533 signal is apparent in the full temperature rate term, primarily due to advection at all four
534 locations. Cooling in the mixed layer was due to vertical diffusion at all four points, with
535 ahead-of-eye-center cooling occurring at points 1, 2, and 3. At point 1 within the
536 upwelling, surface mixed layer cooling stopped once the thermocline reached the bottom
537 of the water column, as the source of cold water was removed (Fig. 15 left middle). At
538 point 2 near RU16, ahead-of-eye-center cooling was caused by vertical diffusion cooling
539 being skewed ahead-of-eye-center. At point 3 in the Cold Pool core, vertical diffusion
540 cooling was also skewed ahead-of-eye-center, with advection warming after eye passage.
541 Finally, at point 4 in the deep water, a deep, cold quiescent bottom allowed for some cold
542 water to entrain into the thick ~200m surface mixed layer ahead-of-eye passage, with an
543 advective signal dominating after eye passage.

544 **3.2.6 Advection vs. Mixing Temperature Response: Barry**

545 The temperature diagnostic equation terms plotted for Irene at four locations in
546 Fig. 15 were also plotted for Barry at five locations in Fig. 16. These five locations are
547 indicated by the large red dots in Fig. 5 and the vertical solid black lines in the left panels
548 of Fig. 11. For Barry, the left panel of Fig. 16 is near ALSN6, the second panel is within
549 the warm strip of water, the third panel is within the Cold Pool core, the fourth is near
550 RU17, and the fifth is in deep water. Again, a tidal advection signal is apparent, with
551 vertical diffusion not exhibiting any tidal cooling/warming signal. Vertical diffusion

552 again caused cooling in the mixed layer except at point 5 in the deep water. Point 5 looks
553 primarily advective with a deep quiescent bottom. At points 1-4 the tidal advection
554 cooling/warming periodicity was modulated by the vertical diffusion cooling, which
555 looks to be skewed ahead-of-eye passage during the greatest shear period (Fig. 12 left).

556 **4. Summary**

557 Baroclinic coastal ocean cooling processes were investigated in detail for
558 Hurricane Irene (2011) and Tropical Storm Barry (2007), two summer TCs, both with
559 rapid ahead-of-eye-center cooling, but with different tracks and occurring at different
560 times in the summer season. Cross-shelf variability in the depth-averaged momentum
561 balance terms demonstrated that the dominant force balance driving the baroclinic
562 circulation was the same across the entire MAB shelf. Cross-shelf variability in the
563 temperature diagnostic equations showed that the resultant ahead-of-eye-center cooling
564 of the surface layer in both storms was dominated by mixing rather than advection.

565 For Irene, it was previously found that cross-shelf two-layer surface to bottom
566 opposing current shear was large and along-shelf surface to bottom shear was small at the
567 RU16 glider location [*Glenn et al.*, 2016]. Here, for Barry, it was found that both the
568 cross- and along-shelf components of the surface to bottom opposing current shear
569 contributed to the mixing and cooling observed at the RU17 glider location. For both
570 storms, analysis of bulk shear (including both cross- and along-shelf shear components)
571 indicated a symmetric 50% ahead and 50% behind eye shear pattern in deep water, but
572 with maximum shear skewed ahead-of-eye-center in the shallow water over the
573 continental shelf. This ahead-of-eye-center skewing of the vertical shear was found to

occur not only due to opposing bottom currents over the shelf before the eye, but also due to weaker winds and a deeper surface layer after the eye.

For Irene, the dominant force balance ahead of eye passage was onshore wind stress balanced by offshore pressure gradient, and the large offshore pressure gradient term stretched across the entire shelf. The wind stress and pressure gradient terms switched directions right after eye passage and eventually the force balance evolved to geostrophic long after the storm. For Barry, the dominant force balance on the shelf ahead of eye passage was modulated by the tides but also had the onshore wind stress term balanced by offshore pressure gradient, and again the large offshore pressure gradient term extended all the way across the shelf. The along-shelf force balance also played a role for Barry, potentially due to the location of the cross section relative to the changing slopes of the bathymetry just north of the Hudson Canyon. In both the cross- and along-shelf directions, independent of the wind forcing, there was a maximum in the pressure gradient and Coriolis terms near the shelf break, which coincided with a warm eddy moving southwestward along the shelf slope front with a geostrophic circulation.

Finally, cross-shelf variability in the temperature change diagnostic terms was investigated. For both storms in the shallow water on the shelf, vertical diffusion was the main cause of the mostly ahead-of-eye-center cooling in the surface mixed layer. Tidal periodicity of cooling/warming was apparent in the combined vertical and horizontal advection terms. Cooling in the surface layer due to vertical diffusion did occur within the coastal upwelling during Irene, and the cooling stopped once the thermocline hit the bottom of the water column as the bottom cold water was also removed. In deep water, vertical diffusion and advection were important drivers of mixed layer cooling for Irene,

whereas for Barry in deep water, advection was the main driver in the periodic and alternating warming/cooling near the surface.

The drivers for the major differences in coastal ocean response between Irene and Barry were storm track, structure, intensity, and time of year. Irene had a more inshore MAB track during the late summer stratified season, whereas Barry was weaker with a farther offshore track during the early summer stratified season. Due to the offshore track, MAB surface winds for Barry had a more along-shelf component than the primarily cross-shelf winds during Irene, leading to both cross- and along-shelf components playing a larger role in the coastal ocean response for Barry, and a primarily cross-shelf response for Irene.

5. Discussion

Glenn et al. [2016] identified 11 summer storms that traversed northeastward across the MAB and that exhibited a range of ahead-of-eye-center cooling. Here, we selected two extreme cases—both with an underwater glider deployed—from this envelope: one with an offshore track and the other with an inshore one. One was near the beginning of the summer stratified season and the other near the end. Indeed, differences in the details exist between the two storm extremes—from the along-shore component playing a larger role in Barry's force balance, to the alternating warming/cooling advective tidal signal playing a larger role in Barry's temperature response. Nevertheless, both storms exhibited a two-layer baroclinic circulation, forced by an offshore pressure gradient opposing the onshore wind stress ahead-of-eye-center and extending across the entire MAB shelf. Cooling in both storms was mostly ahead-of-eye-center and dominated by vertical shear-induced mixing. These commonalities across the two storm extremes

620 indicate that the process is robust and can be expected on stratified continental shelves
621 over a wide range of TC scenarios.
622 Because this process is robust across these two extreme cases drawn from the 30-
623 year envelope of MAB summer cyclones, it will be critical to resolve and forecast the
624 same process for future storms, with the goal of lowering the uncertainty in predictions of
625 TC impacts. Realistic 3D coupled models that assimilate coastal observatory data and
626 that are capable of predicting the ahead-of-eye-center stratified coastal ocean cooling
627 processes will be critical [e.g. *Zambon et al.*, 2014; *Warner et al.*, 2017]. The
628 increasingly populated [*Peduzzi et al.*, 2012] at-risk coastlines—the Northeast U.S. and
629 northeastern China and Korea—adjacent to the two most stratified seas in the world—the
630 MAB and Yellow Sea—will be increasingly vulnerable to TCs as sea levels rise [*Hansen*
631 *et al.*, 2016], as TCs more frequently and severely undergo rapid intensification just
632 before landfall [*Emanuel*, 2016], and if maximum TC intensities continue to migrate
633 poleward [*Kossin et al.*, 2014]. By lowering uncertainty in coastal TC intensity forecasts
634 through models that resolve these stratified coastal ocean cooling processes, these
635 populations can better prepare for and respond to these rising threats.
636
637 **Acknowledgments**
638 HF Radar, glider, and satellite SST data used in this study are available through the
639 MARACOOS assets page http://maracoos.org/data,
640 https://rucool.marine.rutgers.edu/data, and
641 http://marine.rutgers.edu/cool/auvs/index.php?did=369 with more detailed data sets
642 available upon request to gregory.seroka@noaa.gov. Regional Ocean Modeling System

643 results are also available upon request to gregory.seroka@noaa.gov. NAM data sets are
644 publicly available through https://www.ncdc.noaa.gov/data-access/model-data/model-
645 datasets/north-american-mesoscale-forecast-system-nam. Support was provided by New
646 Jersey Board of Public Utilities (2010RU-COOL, BP-070), the Environmental Protection
647 Agency (EP-11-C-000085), New Jersey Department of Environmental Protection
648 (WM13-019-2013), National Oceanic and Atmospheric Administration (NOAA) led
649 Integrated Ocean Observing System through the Mid-Atlantic Regional Association
650 Coastal Ocean Observing System (MARACOOS, NA11NOS0120038), NOAA
651 Cooperative Institute for the North Atlantic Region (NA13OAR4830233), and Rutgers
652 University. We would like to thank John Wilkin and Julia Levin at Rutgers University for
653 their suggestions regarding the ocean modeling, the Rutgers Ocean Modeling research
654 associates for their ROMS help, and Rich Dunk for his helpful meteorological
655 discussions and ideas.

656
657

References

Cangialosi, J. P., and J. L. Franklin (2016), *National Hurricane Center Forecast Verification Report: 2015 Hurricane Season*.

D'Asaro, E., T. B. Sanford, P. P. Niiler, and E. J. Terrill (2007), Cold wake of Hurricane Frances, *Geophys. Res. Lett.*, *34*(15), 2–7, doi:10.1029/2007GL030160.

Davis, R. E., C. C. Eriksen, and C. P. Jones (2002), Autonomous Buoyancy-driven Underwater Gliders, *Technol. Appl. Auton. Underw. Veh.*, 37–58.

DeMaria, M., C. R. Sampson, J. A. Knaff, and K. D. Musgrave (2014), Is tropical cyclone intensity guidance improving?, *Bull. Am. Meteorol. Soc.*, *95*(3), 387–398, doi:10.1175/BAMS-D-12-00240.1.

Emanuel, K. (2016), Will Global Warming Make Hurricane Forecasting More Difficult?, *Bull. Am. Meteorol. Soc.*, doi:10.1175/BAMS-D-16-0134.1.

Fairall, C. W., E. F. Bradley, J. E. Hare, and A. A. Grachev (2003), Bulk parameterization of air-sea fluxes: Updates and verification for the COARE algorithm, *J. Clim.*, *16*(4), 571–591.

Glenn, S., C. Jones, M. Twardowski, L. Bowers, J. Kerfoot, J. Kohut, D. Webb, and O. Schofield (2008), Glider observations of sediment resuspension in a Middle Atlantic Bight fall transition storm, *Limnol. Oceanogr.*, *53*(5 part 2), 2180–2196, doi:10.4319/lo.2008.53.5_part_2.2180.

Glenn, S. M., T. N. Miles, G. N. Seroka, Y. Xu, R. K. Forney, F. Yu, H. Roarty, O. Schofield, and J. Kohut (2016), Stratified Coastal Ocean Interactions with Tropical Cyclones, *Nat. Commun.*, *7*(08 March 2016), doi:10.1038/ncomms10887.

Haidvogel, D. B. et al. (2008), Ocean forecasting in terrain-following coordinates: Formulation and skill assessment of the Regional Ocean Modeling System, *J. Comput. Phys.*, *227*(7), 3595–3624, doi:10.1016/j.jcp.2007.06.016.

Hansen, J. et al. (2016), Ice melt, sea level rise and superstorms: evidence from paleoclimate data, climate modeling, and modern observations that 2◦C global warming could be dangerous, *Atmos. Chem. Phys.*, *16*(6), 3761–3812, doi:10.5194/acp-16-3761-2016.

Houghton, R. W., R. Schlitz, R. C. Beardsley, B. Butman, and J. L. Chamberlin (1982), The Middle Atlantic Bight Cold Pool: Evolution of the Temperature Structure During Summer 1979, *J. Phys. Oceanogr.*, *12*(10), 1019–1029, doi:10.1175/1520-0485.

Hsu, S. A., and Z. Yan (1998), A Note on the Radius of Maximum Wind for Hurricanes, *J. Coast. Res.*, *14*(2), 667–668.

Jaimes, B., and L. K. Shay (2015), Enhanced Wind-Driven Downwelling Flow in Warm Oceanic Eddy Features during the Intensification of Tropical Cyclone Isaac (2012): Observations and Theory, *J. Phys. Oceanogr.*, *45*(6), 1667–1689, doi:10.1175/JPO-D-14-0176.1.

Keen, T. R., and S. M. Glenn (1995), A coupled hydrodynamic-bottom boundary layer model of storm and tidal flow in the Middle Atlantic Bight of North America, *J. Phys. Oceanogr.*, *25*(3), 391–406.

Kim, H. S., C. Lozano, V. Tallapragada, D. Iredell, D. Sheinin, H. L. Tolman, V. M. Gerald, and J. Sims (2014), Performance of ocean simulations in the coupled HWRF-HYCOM model, *J. Atmos. Ocean. Technol.*, *31*(2), 545–559,

doi:10.1175/JTECH-D-13-00013.1.
Kossin, J. P., K. Emanuel, and G. Vecchi (2014), The poleward migration of the location of tropical cyclone maximum intensity., *Nature*, *509*(7500), 349–52, doi:10.1038/nature13278.
Lin, I.-I., C.-H. Chen, I.-F. Pun, W. T. Liu, and C.-C. Wu (2009), Warm ocean anomaly, air sea fluxes, and the rapid intensification of tropical cyclone Nargis (2008), *Geophys. Res. Lett.*, *36*(3), 1–5, doi:10.1029/2008GL035815.
Mei, W., C. Pasquero, and F. Primeau (2012), The effect of translation speed upon the intensity of tropical cyclones over the tropical ocean, *Geophys. Res. Lett.*, *39*(7), 1–6, doi:10.1029/2011GL050765.
Miles, T., S. Glenn, and O. Schofield (2013), Temporal and spatial variability in fall storm induced sediment resuspension on the Mid-Atlantic Bight, *Cont. Shelf Res.*, *63*.
Miles, T. N., G. N. Seroka, J. T. Kohut, O. Schofield, and S. M. Glenn (2015), Glider observations and modeling of sediment transport in Hurricane Sandy, *J. Geophys. Res. Ocean.*, *120*, 1771–1791, doi:10.1002/2014JC010474.Received.
NOAA National Centers for Environmental Prediction (2016), U.S. Coastal Relief Model, Available from: http://www.ngdc.noaa.gov/mgg/coastal/crm.html
Peduzzi, P., B. Chatenoux, H. Dao, A. De Bono, C. Herold, J. Kossin, F. Mouton, and O. Nordbeck (2012), Global trends in tropical cyclone risk, *Nat. Clim. Chang.*, *2*(4), 289–294, doi:10.1038/nclimate1410.
Price, J. F. (1981), Upper Ocean Response to a Hurricane, *J. Phys. Oceanogr.*, *11*(2), 153–175, doi:10.1175/1520-0485(1981)011<0153:UORTAH>2.0.CO;2.
Roarty, H. et al. (2010), Operation and Application of a Regional High-Frequency Radar Network in the Mid-Atlantic Bight, *Mar. Technol. Soc. J.*, *44*(6), 133–145, doi:10.4031/MTSJ.44.6.5.
Ruiz, S., L. Renault, B. Garau, and J. Tintoré (2012), Underwater glider observations and modeling of an abrupt mixing event in the upper ocean, *Geophys. Res. Lett.*, *39*(1), n/a-n/a, doi:10.1029/2011GL050078.
Sampson, C. R., and A. J. Schrader (2000), The Automated Tropical Cyclone Forecasting System (version 3.2), *Bull. Am. Meteorol. Soc.*, *81*(6), 1231–1240, doi:10.1175/1520-0477(2000)081<1231:TATCFS>2.3.CO;2.
Schofield, O. et al. (2007), Slocum Gliders: Robust and ready, *J. F. Robot.*, *24*(6), 473–485, doi:10.1002/rob.20200.
Schofield, O., R. J. Chant, B. Cahill, and R. Castelao (2008), The Decadal View of the Mid-Atlantic Bight from the COOLroom: Is Our Coastal System Changing?, *Oceanography*, *21*(4), 108–117.
Seroka, G. N., T. N. Miles, Y. Xu, J. T. Kohut, O. Schofield, and S. M. Glenn (2016), Hurricane Irene Sensitivity to Stratified Coastal Ocean Cooling, *Mon. Weather Rev.*, *144*(9), 3507–3530, doi:10.1175/MWR-D-15-0452.1.
Sherman, J., R. E. Davis, W. B. Owens, and J. Valdes (2001), The Autonomous Underwater Glider "Spray," *IEEE J. Ocean. Eng.*, *26*(4), 437–446.
Sopko, S. P., and R. J. Falvey (2014), *Annual Tropical Cyclone Report 2014: Joint Typhoon Warning Center*.
Tallapragada, V., C. Kieu, Y. Kwon, S. Trahan, Q. Liu, Z. Zhang, and I.-H. Kwon (2014), Evaluation of Storm Structure from the Operational HWRF during 2012

749 Implementation, *Mon. Weather Rev.*, *142*(11), 4308–4325, doi:10.1175/MWR-D-
750 13-00010.1.
751 Torn, R. D., and C. Snyder (2012), Uncertainty of Tropical Cyclone Best-Track
752 Information, *Weather Forecast.*, *27*(3), 715–729, doi:10.1175/WAF-D-11-00085.1.
753 Umlauf, L., and H. Burchard (2003), A generic length-scale equation for geophysical
754 turbulence models, *J. Mar. Res.*, *61*(2), 235–265,
755 doi:10.1357/002224003322005087.
756 Warner, J. C., C. R. Sherwood, H. G. Arango, and R. P. Signell (2005), Performance of
757 four turbulence closure models implemented using a generic length scale method,
758 *Ocean Model.*, *8*(1–2), 81–113, doi:10.1016/j.ocemod.2003.12.003.
759 Warner, J. C., W. C. Schwab, J. H. List, I. Safak, M. Liste, and W. Baldwin (2017),
760 Inner-shelf ocean dynamics and sea fl oor morphologic changes during Hurricane
761 Sandy, *Cont. Shelf Res.*, *138*(2017), 1–18, doi:10.1016/j.csr.2017.02.003.
762 Wilkin, J. L., and E. J. Hunter (2013), An assessment of the skill of real-time models of
763 Mid-Atlantic Bight continental shelf circulation, *J. Geophys. Res. Ocean.*, *118*(6),
764 2919–2933, doi:10.1002/jgrc.20223.
765 Zambon, J. B., R. He, and J. C. Warner (2014), Tropical to extratropical: Marine
766 environmental changes associated with Superstorm Sandy prior to its landfall,
767 *Geophys. Res. Lett.*, *41*, 8935–8943, doi:10.1002/2014GL061357.Received.
768 Zhang, H., D. Chen, L. Zhou, X. Liu, T. Ding, and B. Zhou (2016), Upper ocean
769 response to typhoon Kalmaegi (2014), *J. Geophys. Res. Ocean.*, *121*(8), 6520–6535,
770 doi:10.1002/2016JC012064.Received.
771 Zhang, W. G., and G. G. Gawarkiewicz (2015), Dynamics of the direct intrusion of Gulf
772 Stream ring water onto the Mid-Atlantic Bight shelf, *Geophys. Res. Lett.*, *42*(18),
773 7687–7695, doi:10.1002/2015GL065530.
774

Figure Captions

Figure 1. Irene and Barry. NHC best track spatial map (left) for Irene (gray solid line) and Barry (black solid line), with position uncertainty circles plotted at each NHC best track position for each storm. NAM in dashed-dotted line for Irene (gray) and Barry (black). 50 and 200m isobaths in dotted contours. Date/time are in format 2011 MM HH:MM for Irene and 2007 MM HH:MM for Barry. NHC best track intensity time series for Irene (top right) and Barry (bottom right), with minimum central pressure (hPa) in solid black line and maximum sustained 10m wind speeds (m s^{-1}) in solid gray line and intensity uncertainty in shaded gray. NAM in black dashed-dotted lines for minimum central pressure and gray dashed-dotted lines for maximum winds. NHC best track position and intensity uncertainties are from [*Torn and Snyder*, 2012] and depend on the intensity of the TC. All times are in UTC.

Figure 2. Irene and Barry. HF radar surface ocean current 1-hour center-averaged maps for Irene and Barry before eye passage by RU16 (Irene, top left) and RU17 (Barry, top right). NHC best track in black, with large black arrow indicating general direction of surface currents. Location of RU16 and RU17 shown with red triangles. Time series at glider locations of temperature with thermocline depth in black contour, transition layer depth (see Glenn et al. [2016] for definitions) in magenta contour, and large white arrows indicating general direction of layer currents (second row from top); cross-shelf currents (third row from top); along-shelf currents (fourth row); and surface to bottom shear for Barry (bottom right). Currents and shear are smoothed using the MATLAB “smooth” function using a span of 8.

799

800 **Figure 3. Irene.** AVHRR Multi-Channel SST (MCSST) (top left) and ROMS ESPreSSO
801 re-run SST (top right) pre-storm for Irene; the same for post-storm in middle panels, and
802 for post-storm minus pre-storm in bottom panels. Dashed magenta contour is 50m
803 isobath, and solid magenta contour is 200m isobath. RU16 location throughout the storm
804 period plotted as yellow triangle, NHC best track for Irene in black with red outlined
805 dots, small black dots in line northwest to southeast indicating cross section location
806 taken for Hövmoller figures below, and large red dots along this black line indicating
807 profile locations taken for temperature diagnostic Fig. 15 below.

808

809 **Figure 4. Irene.** RU16 glider temperature (°C) (left) and ROMS ESPreSSO re-run
810 temperature (°C) (right) at the closest ESPreSSO grid point to the average RU16 glider
811 location during the storm.

812

813 **Figure 5. Barry.** The same as Fig. 3, but for Barry. NDBC station ALSN6 and RU17
814 glider locations indicated with yellow triangles. Northern cross section location used for
815 Barry plotted as west-northwest to east-southeast black dots just north of the Hudson
816 Canyon, and large red dots along this black line indicating profile locations taken for
817 temperature diagnostic Fig. 16 below. A third panel on bottom (bottom right) is added for
818 Barry with post-storm minus pre-storm time difference chosen to maximize the cooling
819 across the map in the ROMS ESPreSSO re-run.

820

Figure 6. Barry. The same as Fig. 4, but for RU17 glider in Barry. RU17 only sampled to ~60m even though full water column depth was >80m.

Figure 7. Irene. Hövmollers of ROMS ESPreSSO re-run SST (°C, top left), surface cross-shelf currents (m s^{-1}, top middle), and surface along-shelf currents (m s^{-1}, top right), with positive reds offshore/northeastward and negative blues onshore/southwestward for cross-shelf/along-shelf currents. Bottom row the same as top row but for the bottom of the water column. Eye passage in NAM atmospheric forcing marked with the horizontal dashed line, and RU16 glider location marked with the vertical dashed line. Vertical solid lines in left panels labeled 1 (upwelling), 2 (near RU16), 3 (in Cold Pool core), and 4 (in deep water) are locations where temperature diagnostics are performed in Fig. 15. Water depth (m) along the cross section is plotted in the panels below the Hövmoller panels.

Figure 8. Irene. Same formatted Hövmoller as in Fig. 7, but for bulk surface to bottom cross- and along-shelf shear (left, m s^{-1}). This bulk shear is calculated according to the equation in the header: square root of the sum of the squares of the surface to bottom cross- and along-shelf shears. Right panel is the same as left but for 0 substituted for bottom currents.

Figure 9. Irene. Hövmollers of the cross-shelf depth-averaged momentum balance terms (m s^{-2}), with positive reds offshore and negative blues onshore. Horizontal diffusion was small and thus not plotted.

844 **Figure 10. Irene.** Same as Fig. 9 but for along-shelf depth-averaged momentum balance
845 terms (m s^{-2}), with positive reds northeastward and negative blues southwestward.
846
847 **Figure 11. Barry.** Same as Fig. 7 but for Barry, with ALSN6 and RU17 locations plotted
848 as vertical dashed lines. Vertical solid lines in left panels labeled 2 (near ALSN6), 2 (in
849 warm strip), 3 (in Cold Pool core), 4 (near RU17), and 5 (in deep water) are locations
850 where temperature diagnostics are performed in Fig. 16.
851
852 **Figure 12. Barry.** Same as Fig. 8 (bulk surface to bottom shear analysis), but for Barry.
853
854 **Figure 13. Barry.** Same as Fig. 9 (Hövmoller cross-shelf depth-averaged momentum
855 balance terms), but for Barry.
856
857 **Figure 14. Barry.** Same as Fig. 10 (Hövmoller along-shelf depth-averaged momentum
858 balance terms), but for Barry.
859
860 **Figure 15. Irene.** Temperature diagnostic equation terms at points 1-4 marked in Fig. 3's
861 red dots ordered 1-4 northwest to southeast, and in Fig. 7's left panels, with full
862 temperature rate term at top, vertical diffusion in middle, and vertical + horizontal
863 advection at bottom (°C s^{-1}). Horizontal diffusion is small and thus not plotted. Eye
864 passage marked with vertical dashed line. At point 4, only the top 500m of the water
865 column is plotted.
866

867 **Figure 16. Barry.** Same as Fig. 15 (temperature diagnostic equation terms) but for Barry.
868 Points 1-5 are marked in Fig. 5's red dots ordered 1-5 west-northwest to east-southeast,
869 and in Fig. 11's left panels.
870

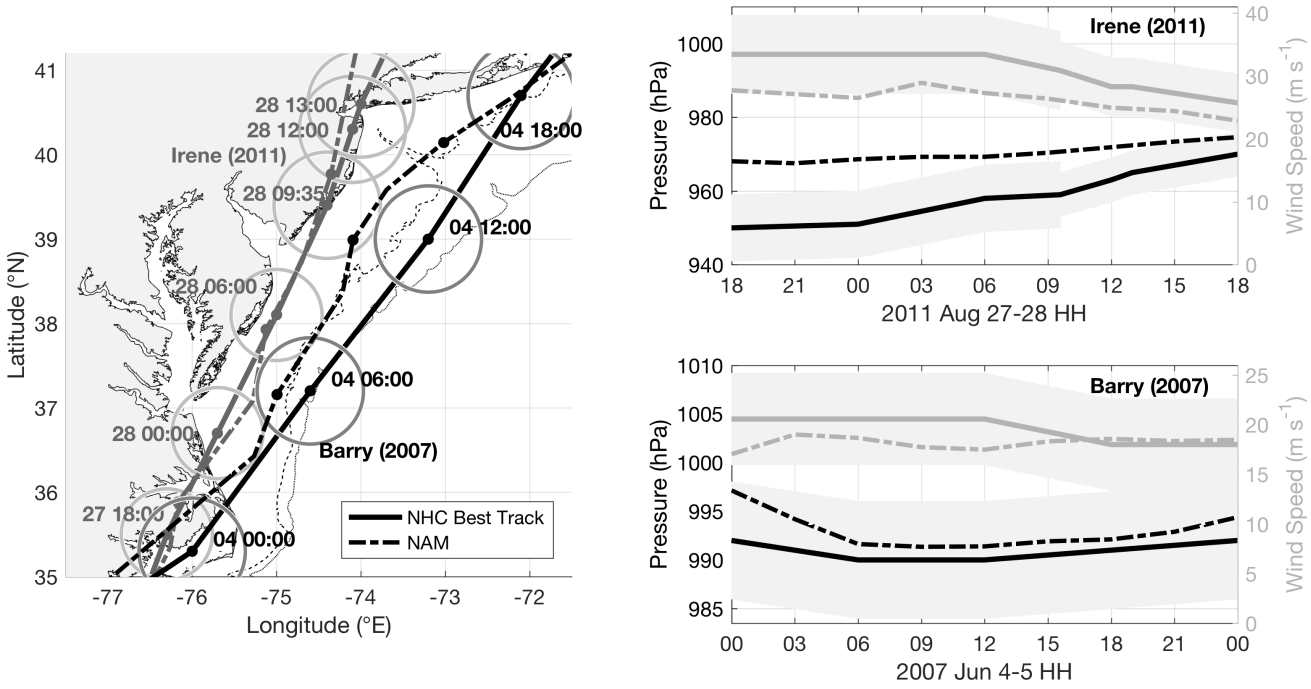

871 **Figure 1. Irene and Barry.** NHC best track spatial map (left) for Irene (gray solid line)
872 and Barry (black solid line), with position uncertainty circles plotted at each NHC best
873 track position for each storm. NAM in dashed-dotted line for Irene (gray) and Barry
874 (black). 50 and 200m isobaths in dotted contours. Date/time are in format 2011 MM
875 HH:MM for Irene and 2007 MM HH:MM for Barry. NHC best track intensity time series
876 for Irene (top right) and Barry (bottom right), with minimum central pressure (hPa) in
877 solid black line and maximum sustained 10m wind speeds (m s^{-1}) in solid gray line and
878 intensity uncertainty in shaded gray. NAM in black dashed-dotted lines for minimum
879 central pressure and gray dashed-dotted lines for maximum winds. NHC best track
880 position and intensity uncertainties are from [*Torn and Snyder*, 2012] and depend on the
881 intensity of the TC. All times are in UTC.

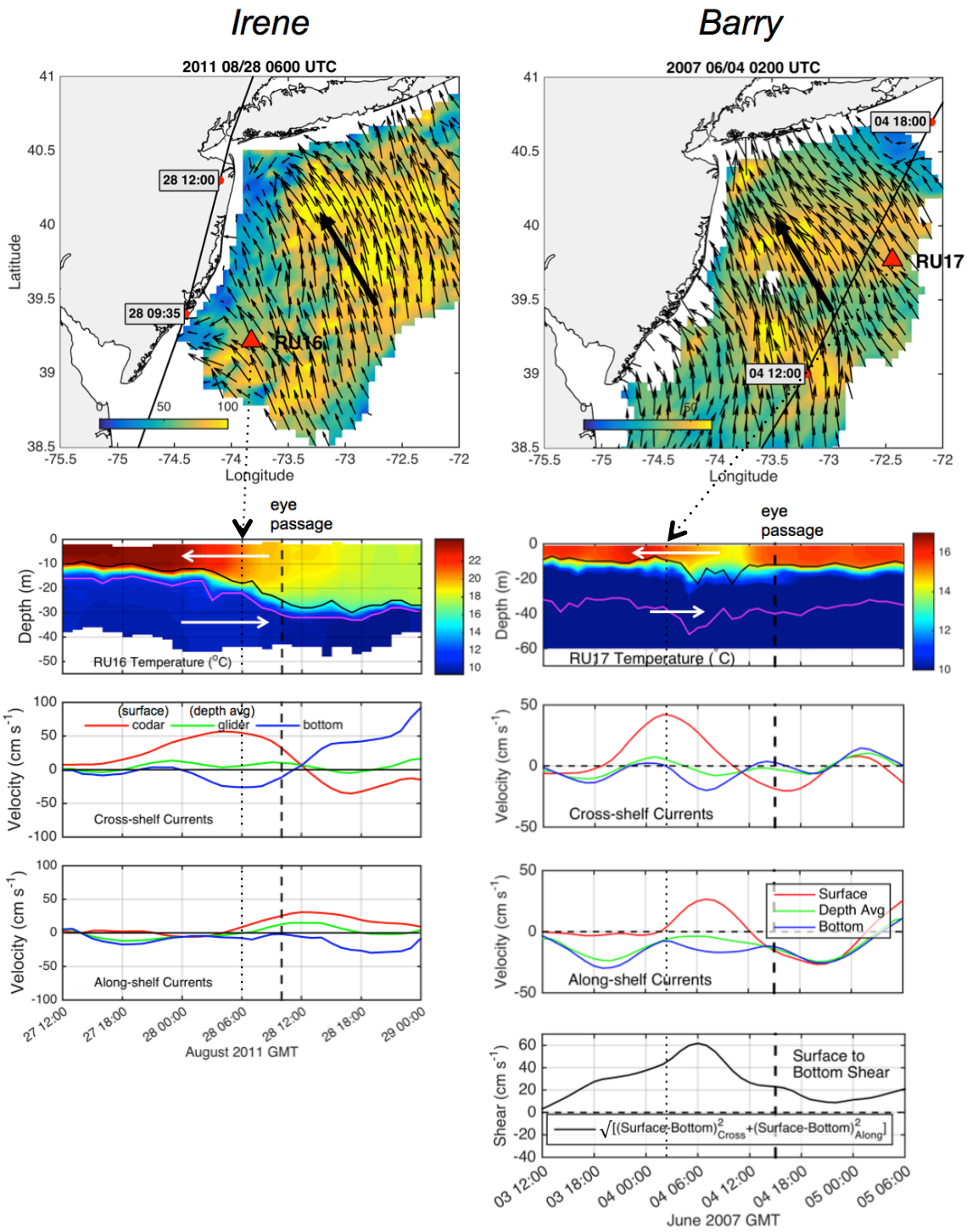

Figure 2. Irene and Barry. HF radar surface ocean current 1-hour center-averaged maps for Irene and Barry before eye passage by RU16 (Irene, top left) and RU17 (Barry, top right). NHC best track in black, with large black arrow indicating general direction of surface currents. Location of RU16 and RU17 shown with red triangles. Time series at glider locations of temperature with thermocline depth in black contour, transition layer depth (see Glenn et al. [2016] for definitions) in magenta contour, and large white arrows indicating general direction of layer currents (second row from top); cross-shelf

currents (third row from top); along-shelf currents (fourth row); and surface to bottom shear for Barry (bottom right). Currents and shear are smoothed using the MATLAB "smooth" function using a span of 8.

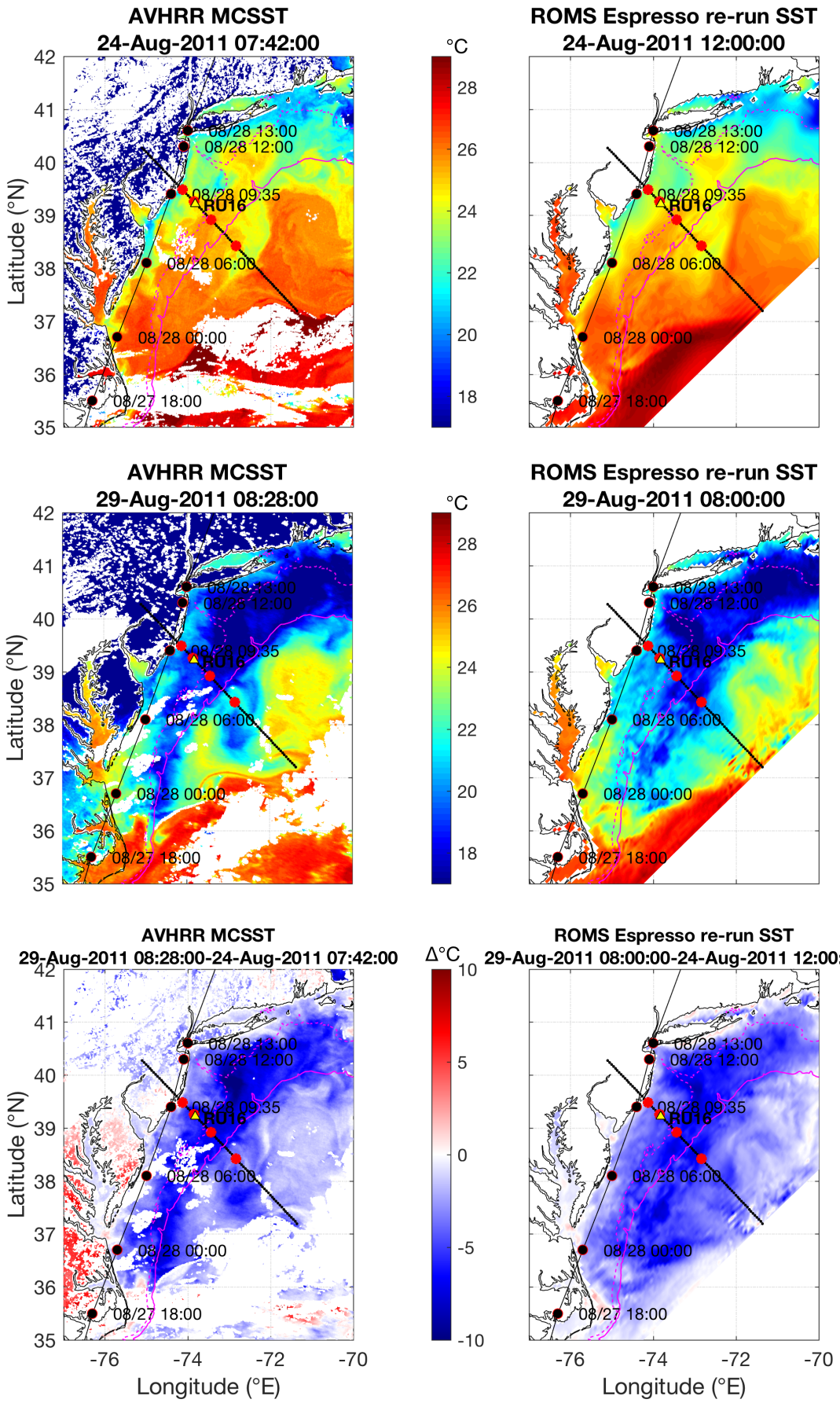
AVHRR MCSST
24-Aug-2011 07:42:00
ROMS Espresso re-run SST
24-Aug-2011 12:00:00
°C
AVHRR MCSST
29-Aug-2011 08:28:00
ROMS Espresso re-run SST
29-Aug-2011 08:00:00
°C
AVHRR MCSST
29-Aug-2011 08:28:00-24-Aug-2011 07:42:00
ROMS Espresso re-run SST
29-Aug-2011 08:00:00-24-Aug-2011 12:00:00
Δ°C
08/28 13:00
08/28 12:00
08/28 09:35
RU16
08/28 06:00
08/28 00:00
08/27 18:00
Latitude (°N)
Longitude (°E)

Figure 3. Irene. AVHRR Multi-Channel SST (MCSST) (top left) and ROMS ESPreSSO re-run SST (top right) pre-storm for Irene; the same for post-storm in middle panels, and for post-storm minus pre-storm in bottom panels. Dashed magenta contour is 50m isobath, and solid magenta contour is 200m isobath. RU16 location throughout the storm period plotted as yellow triangle, NHC best track for Irene in black with red outlined dots, small black dots in line northwest to southeast indicating cross section location taken for Hövmoller figures below, and large red dots along this black line indicating profile locations taken for temperature diagnostic Fig. 15 below.

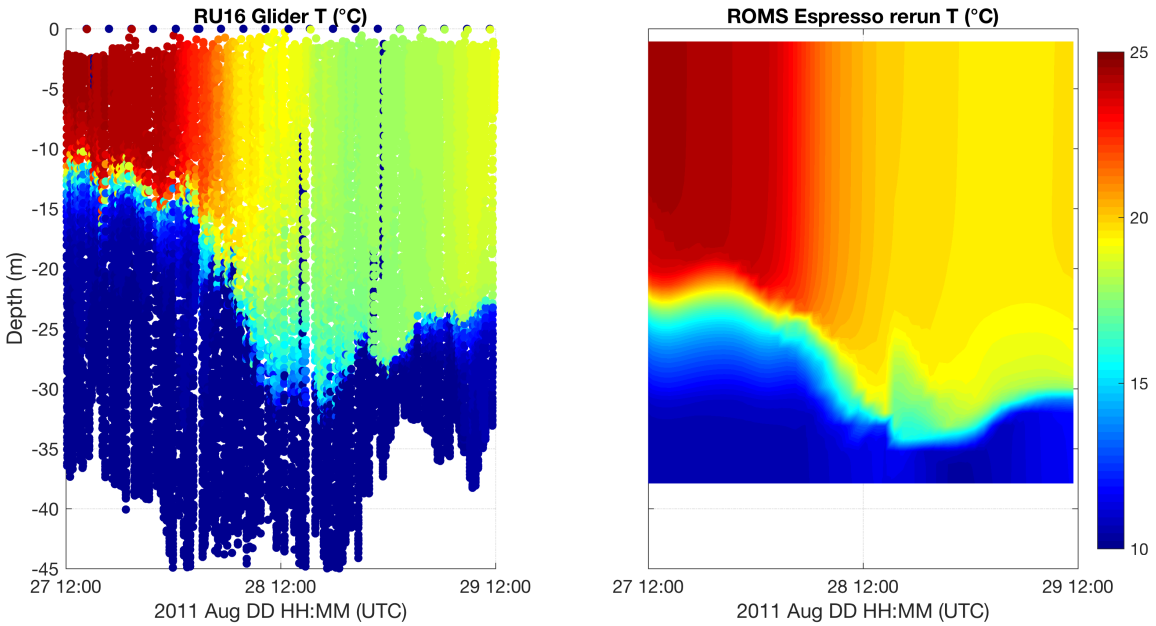

Figure 4. Irene. RU16 glider temperature (°C) (left) and ROMS ESPreSSO re-run temperature (°C) (right) at the closest ESPreSSO grid point to the average RU16 glider location during the storm.

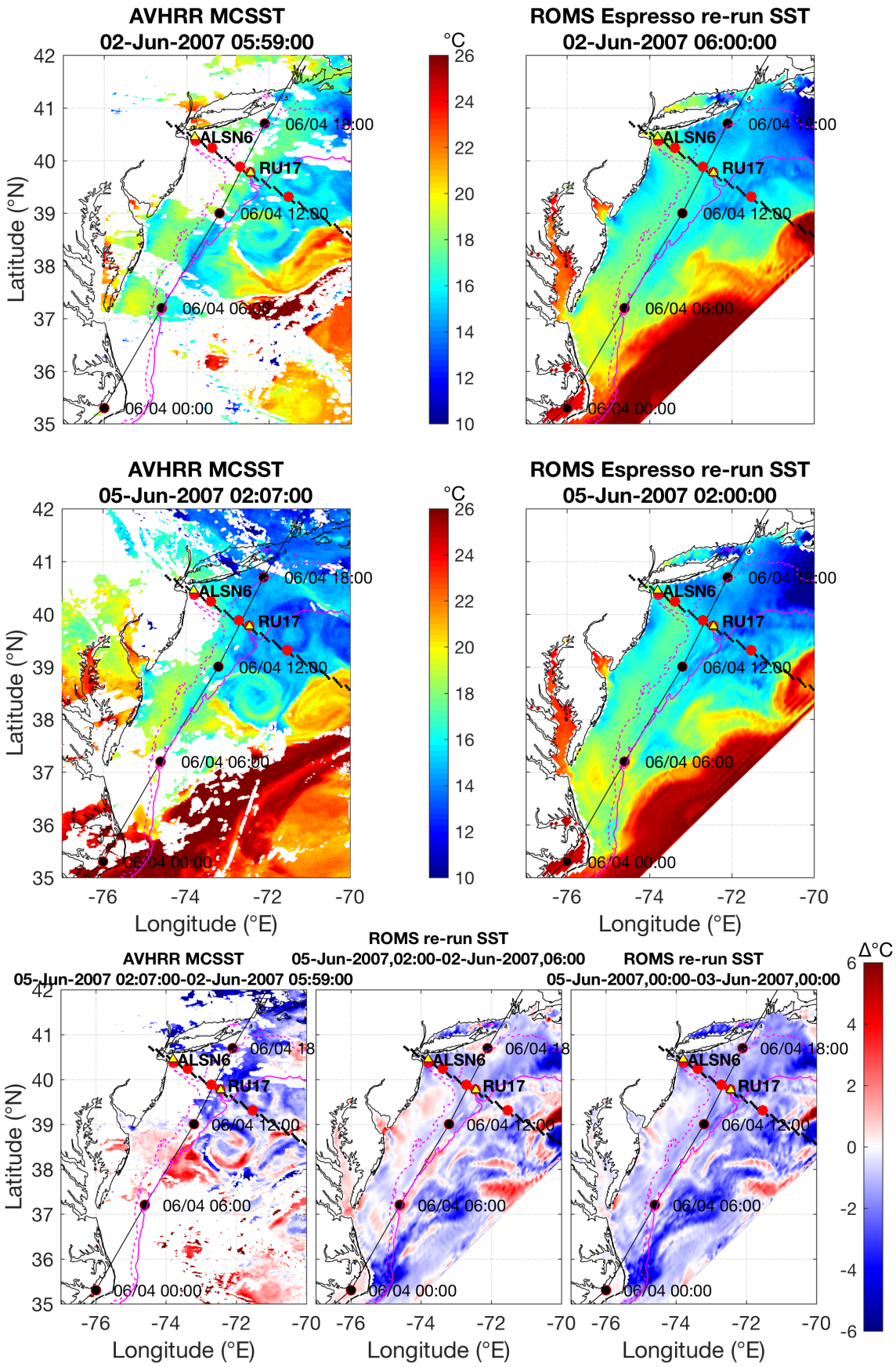
AVHRR MCSST
02-Jun-2007 05:59:00
ROMS Espresso re-run SST
02-Jun-2007 06:00:00
AVHRR MCSST
05-Jun-2007 02:07:00
ROMS Espresso re-run SST
05-Jun-2007 02:00:00
°C
ALSN6
RU17
06/04 18:00
06/04 12:00
06/04 06:00
06/04 00:00
Latitude (°N)
Longitude (°E)
ROMS re-run SST
AVHRR MCSST
05-Jun-2007 02:07:00-02-Jun-2007 05:59:00
05-Jun-2007,02:00-02-Jun-2007,06:00
ROMS re-run SST
05-Jun-2007,00:00-03-Jun-2007,00:00
Δ°C

914

915 **Figure 5. Barry.** The same as Fig. 3, but for Barry. NDBC station ALSN6 and RU17
916 glider locations indicated with yellow triangles. Northern cross section location used for
917 Barry plotted as west-northwest to east-southeast black dots just north of the Hudson
918 Canyon, and large red dots along this black line indicating profile locations taken for
919 temperature diagnostic Fig. 16 below. A third panel on bottom (bottom right) is added for
920 Barry with post-storm minus pre-storm time difference chosen to maximize the cooling
921 across the map in the ROMS ESPreSSO re-run.
922
923

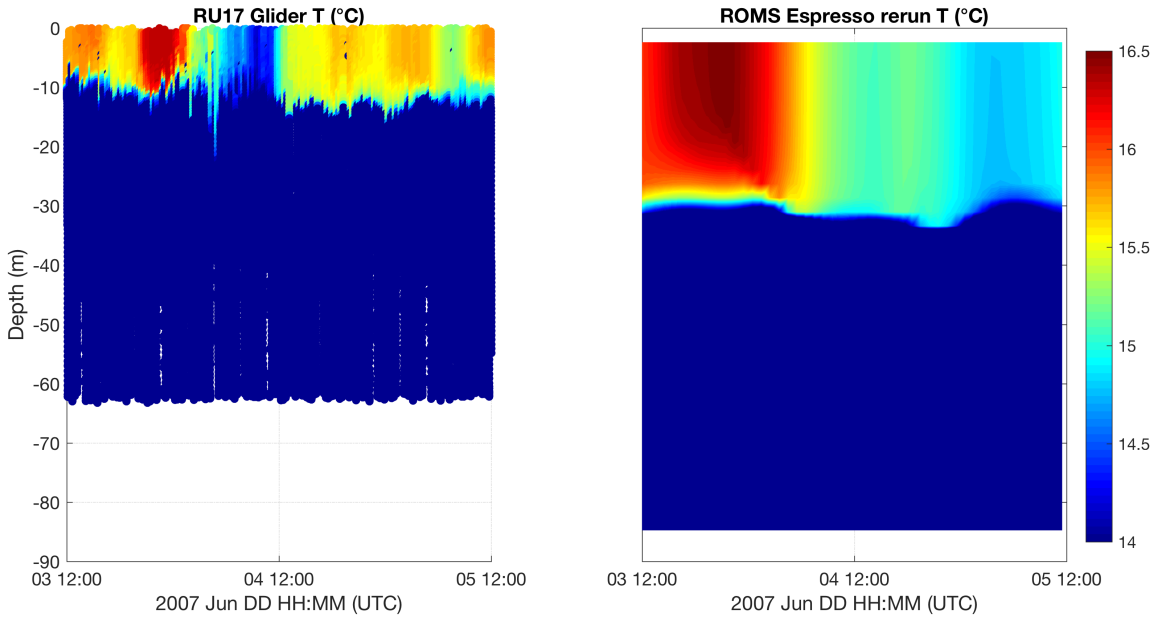

Figure 6. Barry. The same as Fig. 4, but for RU17 glider in Barry. RU17 only sampled to ~60m even though full water column depth was >80m.

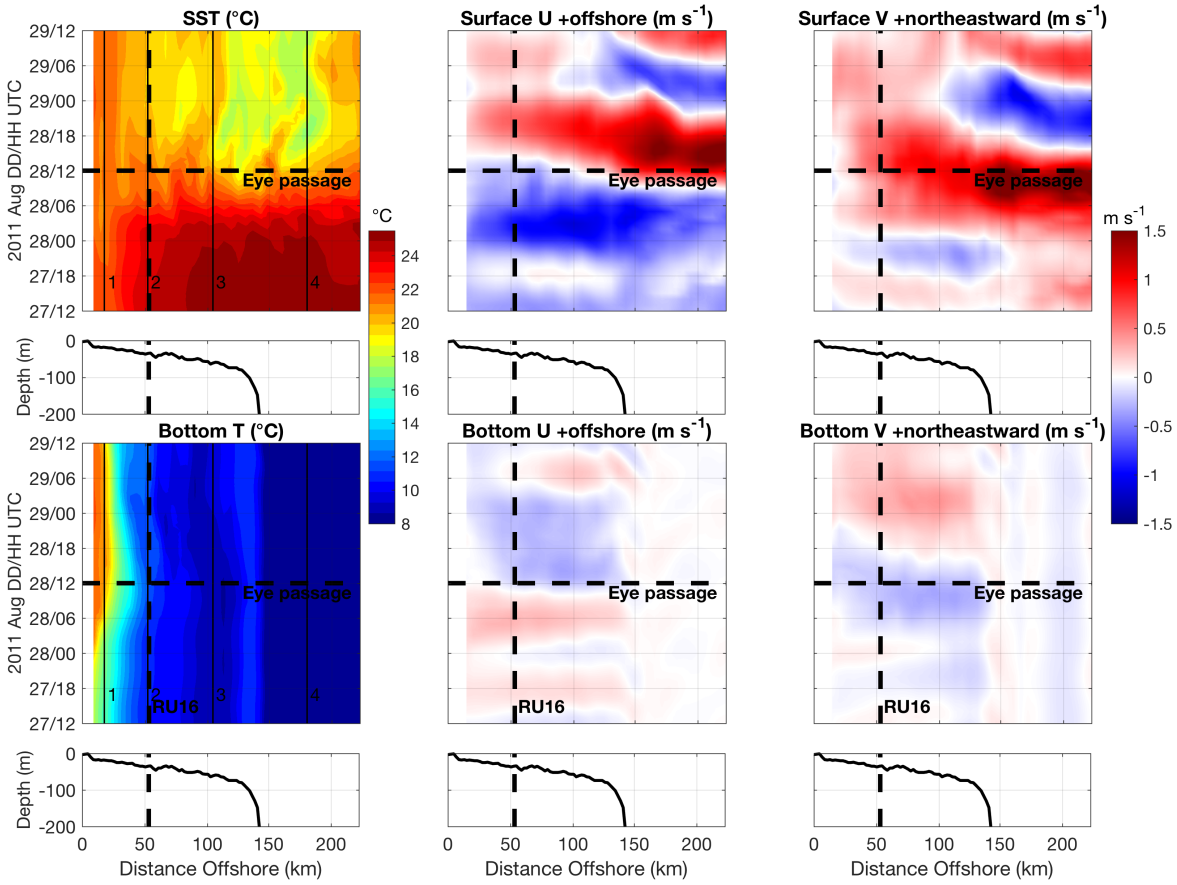

Figure 7. Irene. Hövmollers of ROMS ESPreSSO re-run SST (°C, top left), surface cross-shelf currents (m s^{-1}, top middle), and surface along-shelf currents (m s^{-1}, top right), with positive reds offshore/northeastward and negative blues onshore/southwestward for cross-shelf/along-shelf currents. Bottom row the same as top row but for the bottom of the water column. Eye passage in NAM atmospheric forcing marked with the horizontal dashed line, and RU16 glider location marked with the vertical dashed line. Vertical solid lines in left panels labeled 1 (upwelling), 2 (near RU16), 3 (in Cold Pool core), and 4 (in deep water) are locations where temperature diagnostics are performed in Fig. 15. Water depth (m) along the cross section is plotted in the panels below the Hövmoller panels.

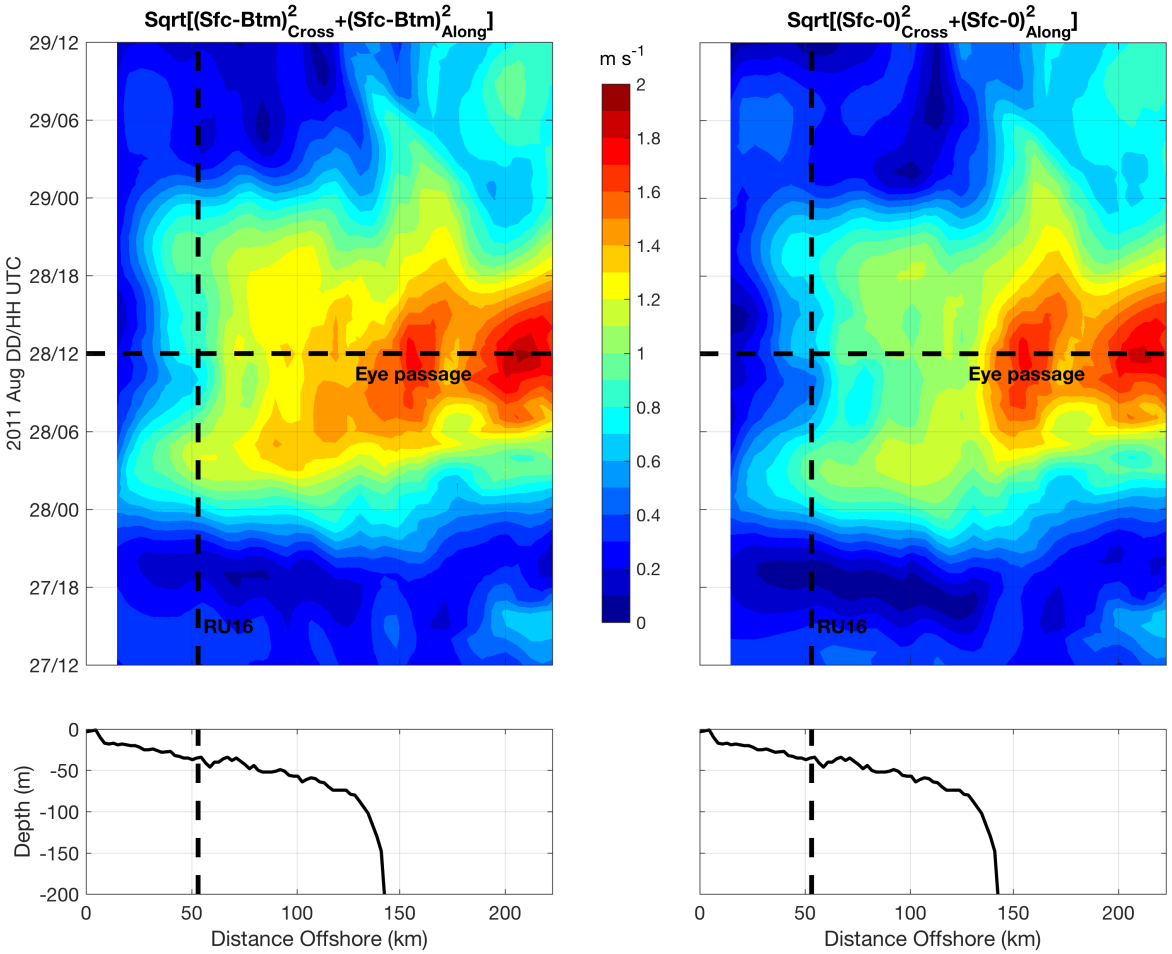

Figure 8. Irene. Same formatted Hövmoller as in Fig. 7, but for bulk surface to bottom cross- and along-shelf shear (left, m s^{-1}). This bulk shear is calculated according to the equation in the header: square root of the sum of the squares of the surface to bottom cross- and along-shelf shears. Right panel is the same as left but for 0 substituted for bottom currents.

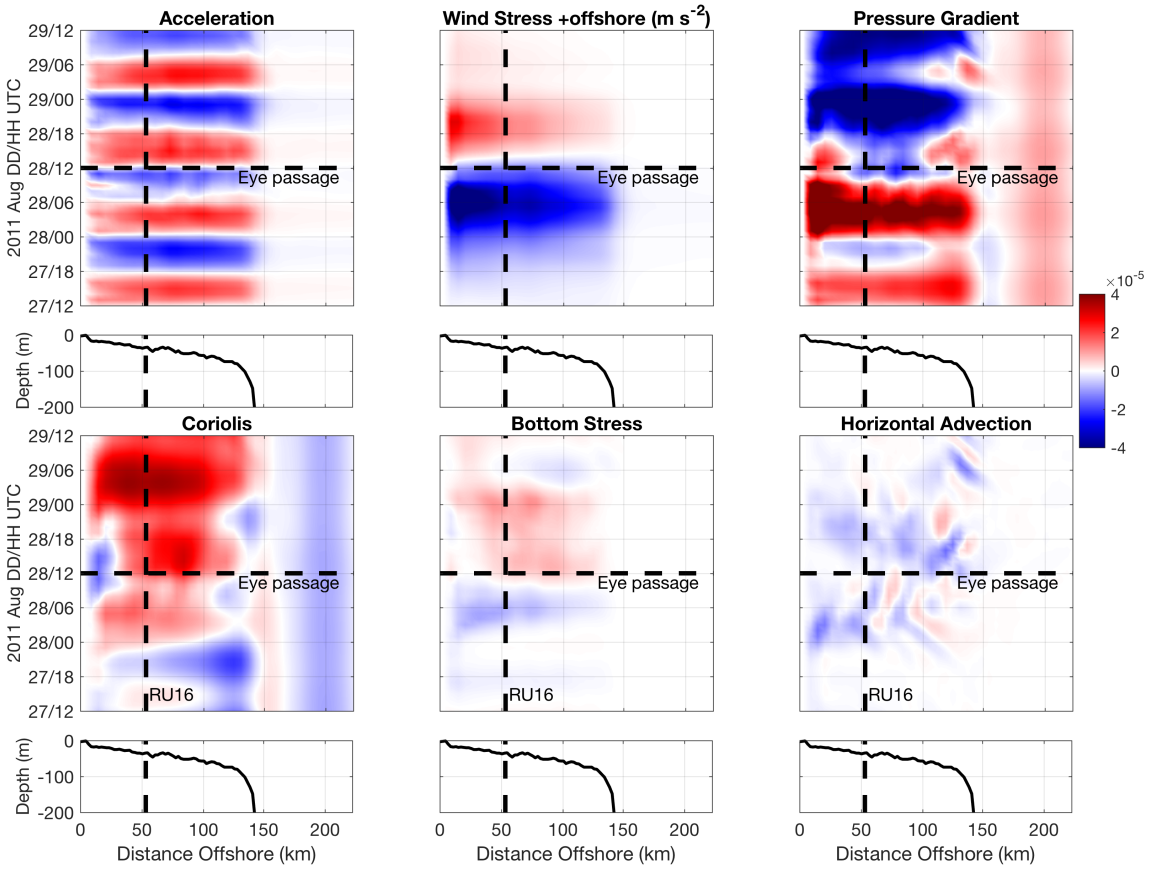

Figure 9. Irene. Hövmollers of the cross-shelf depth-averaged momentum balance terms (m s^{-2}), with positive reds offshore and negative blues onshore. Horizontal diffusion was small and thus not plotted.

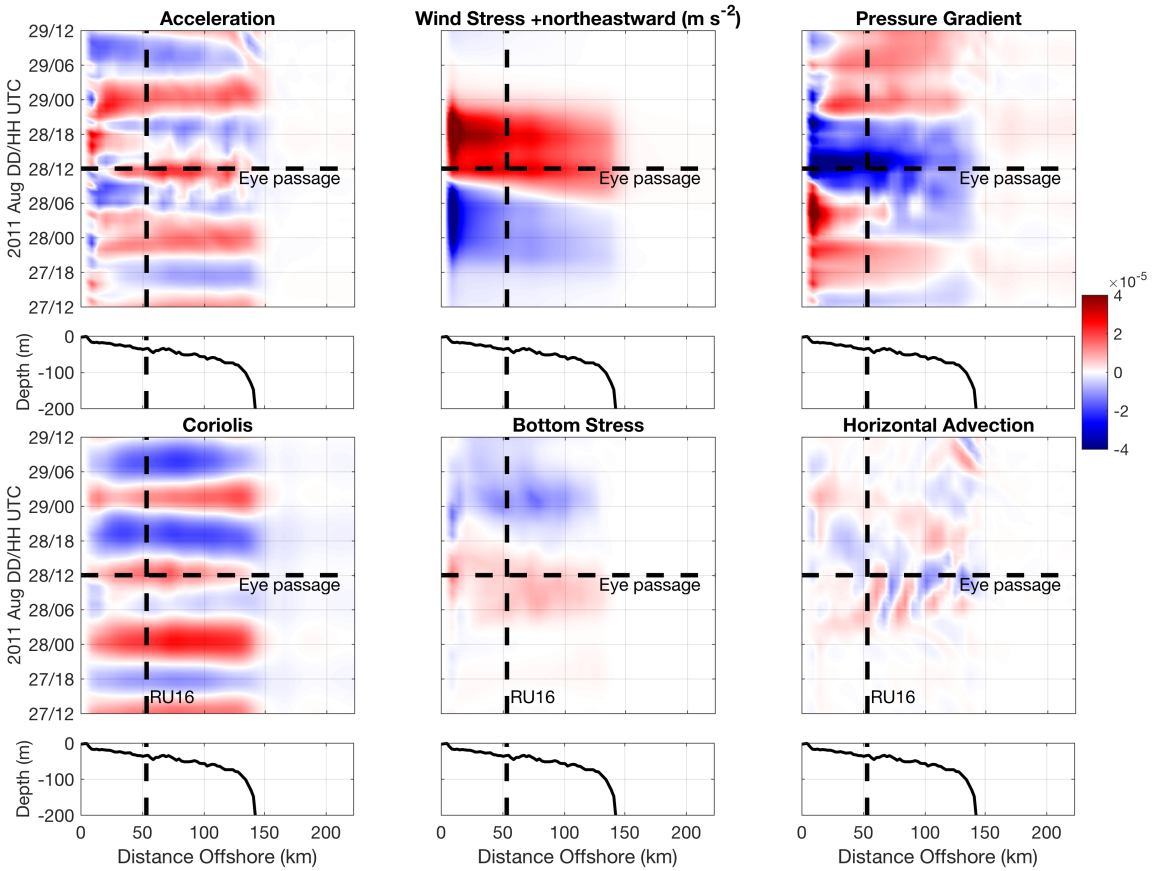

957
958 **Figure 10. Irene.** Same as Fig. 9 but for along-shelf depth-averaged momentum balance
959 terms (m s^{-2}), with positive reds northeastward and negative blues southwestward.
960
961

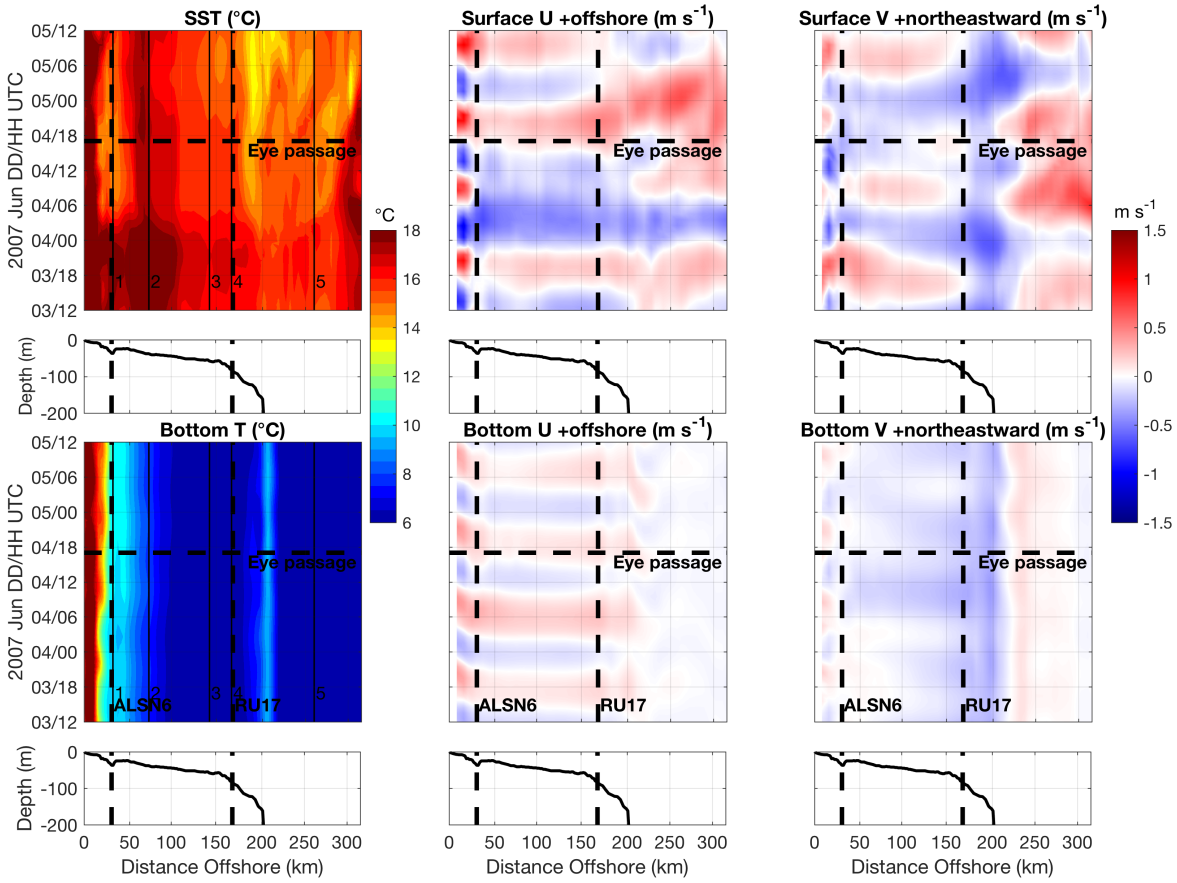

Figure 11. Barry. Same as Fig. 7 but for Barry, with ALSN6 and RU17 locations plotted as vertical dashed lines. Vertical solid lines in left panels labeled 2 (near ALSN6), 2 (in warm strip), 3 (in Cold Pool core), 4 (near RU17), and 5 (in deep water) are locations where temperature diagnostics are performed in Fig. 16.

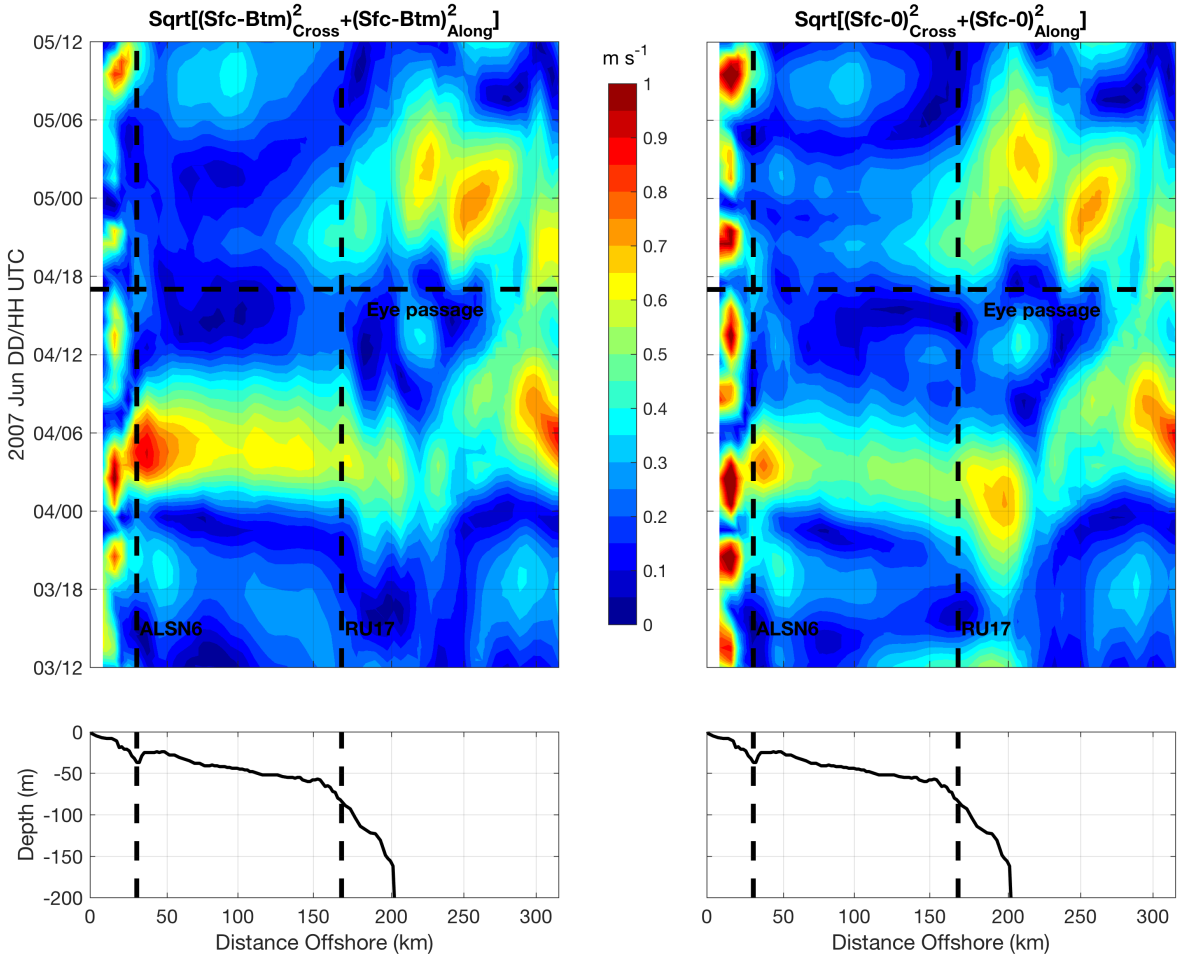

Figure 12. Barry. Same as Fig. 8 (bulk surface to bottom shear analysis), but for Barry.

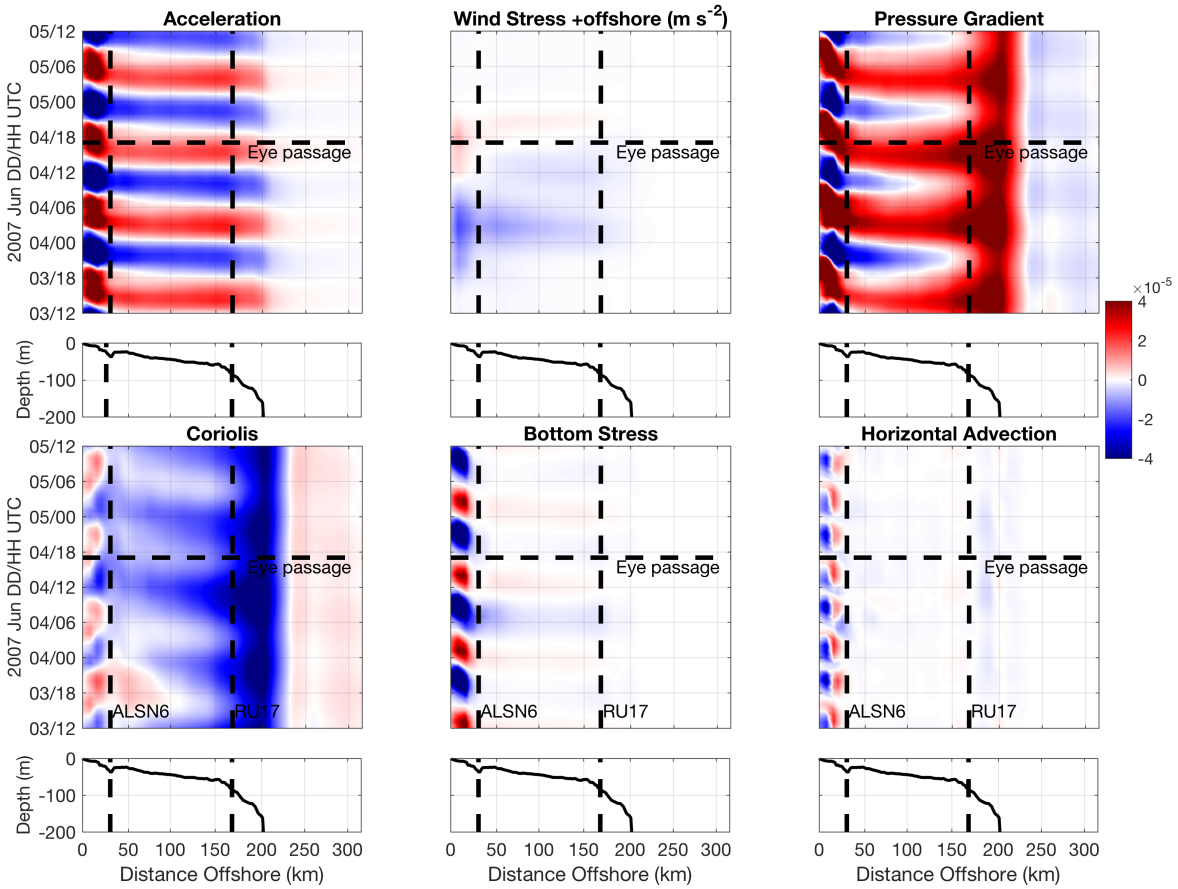

Figure 13. Barry. Same as Fig. 9 (Hövmoller cross-shelf depth-averaged momentum balance terms) but for Barry.

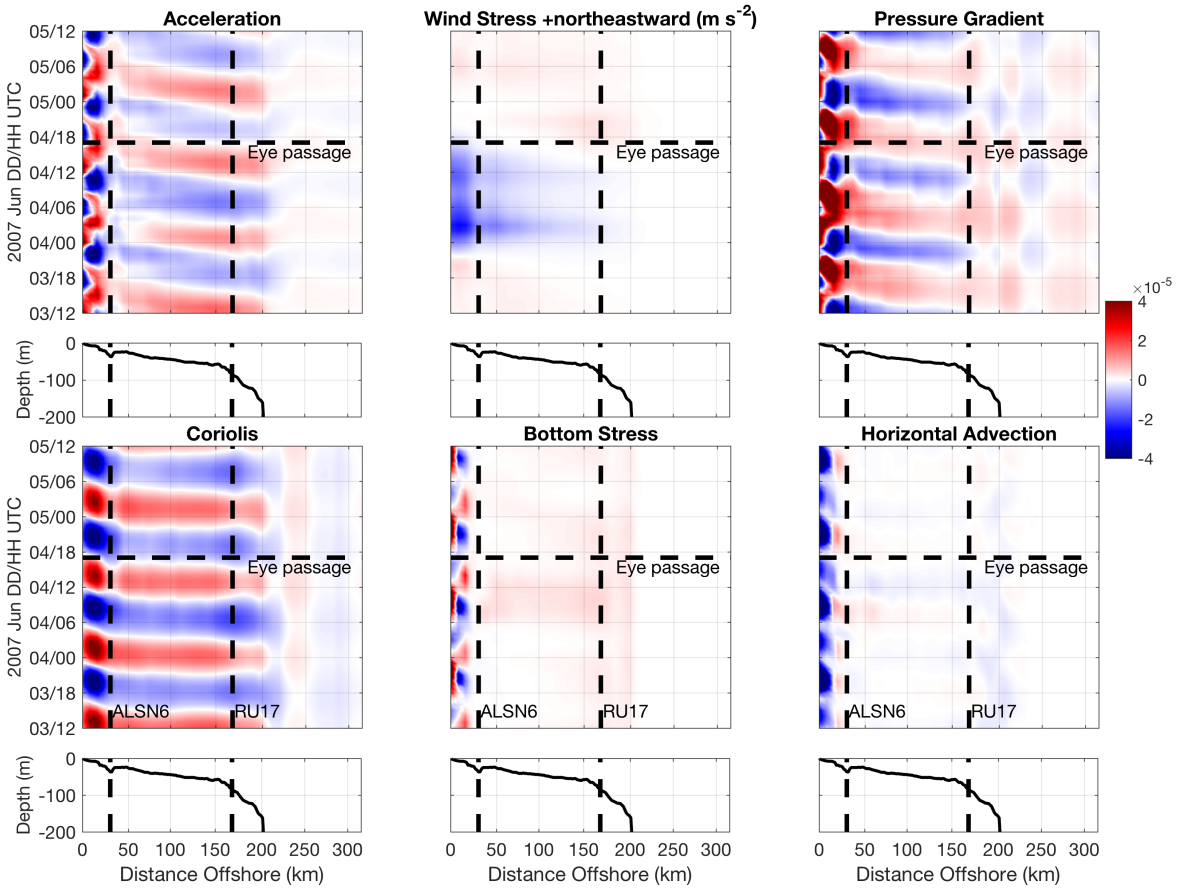

Figure 14. Barry. Same as Fig. 10 (Hövmoller along-shelf depth-averaged momentum balance terms) but for Barry.

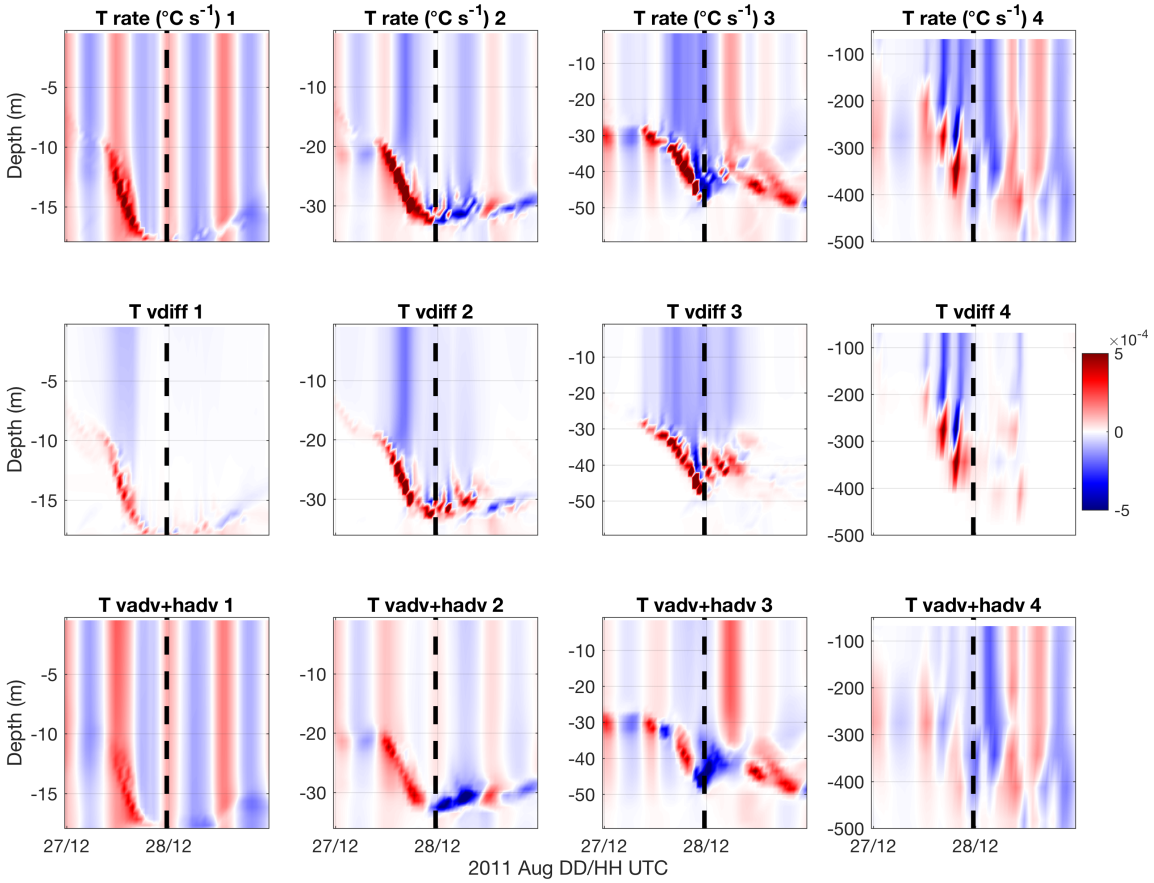

983
984 **Figure 15. Irene.** Temperature diagnostic equation terms at points 1-4 marked in Fig. 3's
985 red dots ordered 1-4 northwest to southeast, and in Fig. 7's left panels, with full
986 temperature rate term at top, vertical diffusion in middle, and vertical + horizontal
987 advection at bottom (°C s^{-1}). Horizontal diffusion is small and thus not plotted. Eye
988 passage marked with vertical dashed line. At point 4, only the top 500m of the water
989 column is plotted.
990
991

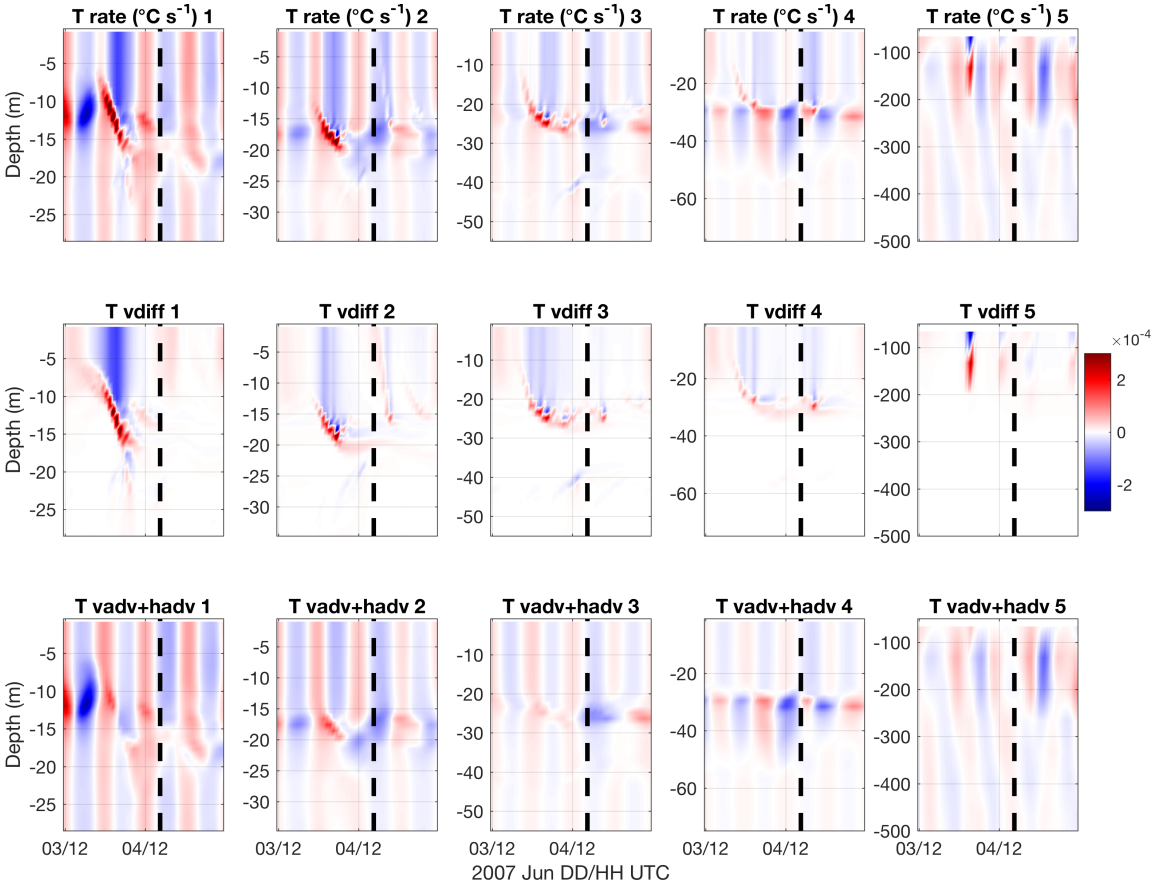

Figure 16. Barry. Same as Fig. 15 (temperature diagnostic equation terms) but for Barry. Points 1-5 are marked in Fig. 5's red dots ordered 1-5 west-northwest to east-southeast, and in Fig. 11's left panels.